Low Temperature Physics/Fizika Nizkikh Temperatur, 2021, vol. 47, No. 5, pp. 387–408

Magnetotransport properties of CrO_2 powder composites

(Review Article)

E. Yu. Beliayev, V. A. Horielyi, and Yu. A. Kolesnichenko

B. Verkin Institute for Low Temperature Physics and Engineering of the National Academy of Sciences of Ukraine
Kharkiv 61103, Ukraine
E-mail: beliayev@ilt.kharkov.ua

Received December 12, 2020, published online March 26, 2021

The most significant experimental results and theoretical concepts related to chromium dioxide-based composites, according to their influence on the evolution of modern understanding of electron transport phenomena in disordered magnetic systems, are presented. It is shown that the variety of physical processes taking place in powder materials does not allow the development of a holistic theoretical approach to describing the properties of the obtained compacted materials. The properties of composite materials depend on the anisotropy of the shape and magnetic properties of particles of which they are composed. The influence of percolation effects leads to a change in the current-carrying channels morphology with the temperature variation in an external magnetic field. This affects both the shape of the magnetoresistance hysteresis loops and the magnetic field magnitudes corresponding to the magnetoresistance maxima. A wide range of magnetotransport phenomena observed in half-metal composite materials contributes to the development of modern concepts of the conductivity features near the metal–insulator threshold and the influence of the metal–insulator interfaces on tunneling conductivity.

Keywords: half-metals, chromium dioxide, magnetic tunnel contacts, pressed powders, percolation conductivity, magnetoresistance anisotropy.

Contents

1. Introduction ... 388
1.1. Prospects for the use of half-metal powder composites in spintronics ... 388
1.2. Giant magnetoresistance in FNF structures ... 388
1.3. Tunnel magnetoresistance of FIF′ structures ... 389
1.4. Tunneling Hamiltonian approximation ... 389
1.5. Slonchevsky formula ... 390
2. Half-metals ... 390
2.1. Half-metals as a special class of ferromagnets ... 390
2.2. Classification of half-metals ... 391
3. Chromium dioxide as a type I_A half-metal ... 392
4. Magnetic properties of CrO_2 ... 393
5. Resistive properties of CrO_2 ... 394
6. Magnetoresistive properties of CrO_2 ... 395
7. Tunneling magnetoresistance in cooperative systems of magnetic tunnel junctions ... 399
8. Percolation conductivity of granular half-metal systems ... 400
9. Anisotropic magnetoresistance in compacted powder composites ... 405
Conclusion ... 406
References ... 406

1. Introduction

1.1. Prospects for the use of half-metal powder composites in spintronics

The dependence of the transport properties of charge carriers in half-metals on the spin degrees of freedom makes it promising to use the electron spin as an active element for storing, processing, and transmitting the information. Currently, there are three main directions for the development of prospective spin-dependent electronic devices: a quantum computer, a spin field-effect transistor, and spin elements of memory. The problem of controlling the spin degrees of freedom is closely related to the search and use the functional materials with high degrees of spin polarization P of conduction electrons, which is usually determined by the simple expression:

$$P = \frac{\rho^{\uparrow}(\varepsilon_F) - \rho^{\downarrow}(\varepsilon_F)}{\rho^{\uparrow}(\varepsilon_F) + \rho^{\downarrow}(\varepsilon_F)}, \qquad (1)$$

where $\rho^{\uparrow\downarrow}(\varepsilon_F)$ is the density of states (DOS) for electrons with the selected spin direction at the Fermi energy level. Possible refinements of definition (1) as applied to transport phenomena are discussed in more details in the theoretical work [1]. In addition, the attention of researchers is attracted to the study of the effects of spin-dependent electron tunneling in cooperative systems consisting of a large number of magnetic tunnel contacts of the same type.

In practical terms, one of the advantages of such systems is the possibility of efficiently control powerful spin-polarized currents. On the other hand, compressed nanopowders, in which ferromagnetic (FM) granules are separated by thin dielectric layers, forming an extensive network of magnetic tunnel junctions, are promising materials for studying the features of spin-dependent electron transport using composite materials as experimental samples. In such samples, dielectric layers (which, in the case of chromium dioxide, can be formed on the surface of CrO_2 granules by partial surface reduction to sesquioxide Cr_2O_3 or chromium oxyhydroxide β-CrOOH) act as tunnel barriers, and the resistance of such system depends both on the direction of magnetization of neighboring granules and on the degree of spin polarization of conduction electrons near the contacts.

From a theoretical point of view, the magnetoresistance (MR) of a granular system of FM particles is determined by the resistance of the electrical contacts between adjacent granules. These can be ohmic contacts between two ferromagnetic metals (FF′), contacts through a nonmagnetic conductor (FNF′), or tunnel contacts through thin insulating barriers (FIF′). The last two electrical connection groups are the most exciting and essential for their future applications in spintronics. In the next two sections, we will briefly discuss the physical processes in relatively simple three-layer systems, which can serve as a model of individual contacts in a cooperative system.

1.2. Giant magnetoresistance in FNF structures

Intensive studies of spin-dependent electron transport followed the discovery in 1988 of the effect of giant magnetoresistance (GMR) in superlattices consisting of alternating thin ferromagnetic (F) and nonmagnetic (N) metallic layers [2, 3]. Firth and Grünberg were awarded the Nobel Prize in Physics in 2007 for the finding and explanation of the GMR effect in multilayers. This discovery marked the beginning of studies of the influence of spin on the electron mobility in complex ...FNFN... multilayer systems, and the practical application of the GMR effect in the read heads of hard disks led to a significant increase in the storage areal density. Systems in which an external magnetic field can control the resistance are called spin valves. The simplest example of a spin valve consists of two ferromagnetic layers separated by a nonmagnetic interlayer. The direction of the magnetic moment of one of the FM layers is determined by an antiferromagnetic (AF) substrate that fixes the direction of its magnetic moment (Fig. 1). The magnetization of the second FM layer can be changed by an external magnetic field. In the case of the antiparallel orientation of the FM layers magnetization, electrons with the chosen spin direction are strongly scattered at one of the boundaries of the nonmagnetic metal with the FM, which determines the high-impedance state of the system. On the contrary, in a parallel configuration, electrons with the spin direction antiparallel to the magnetization of the layers are weakly scattered at the boundaries, forming a channel of high charge carrier mobility that leads to a low-impedance state of the structure. The relative difference between the resistances for parallel and antiparallel orientations of the magnetization in the spin valve structure can reach 30–50% in magnetic fields of ~ 1–5 Oe. Thus, the GMR effect in FNF′ structures is explained by the polarization of the spins of charge carriers due to the exchange interaction when they pass through the FM layers of the magnetic structure and spin-dependent scattering at the boundaries of the magnetic and nonmagnetic layers.

The magnetoresistance of multilayer ...FNF... conductors has been studied theoretically in many works (see, for example, [4–9]). A GMR phenomenon is used in various spintronic devices and is observed in multilayer structures in which the magnetic layers are separated by nonmagnetic interlayers 10–20 Å thick [10]. Other examples of spin-valve systems are structures in which FM layers are separated by a thin dielectric layer.

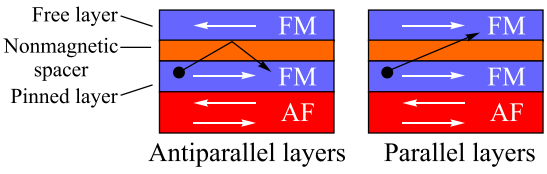

Fig. 1. How the spin valve works.

1.3. Tunnel magnetoresistance of FIF′ structures

The tunneling magnetoresistance effect was first discovered in 1975 by Michel Julliere at a temperature of 4.2 K [11]. The simplest magnetic tunnel structure consists of two layers of FM metal (F), between which there is an insulating layer (I). The magnitude of the current through the magnetic tunnel contact is determined by both the FM electrodes electronic structure and the characteristics of the potential barrier between them. In the paper [11], based on simple physical considerations and suggesting that the electron spin is conserved during tunneling, it was found that the relative change of the tunneling conductance $(G_P–G_{AP})/G_P = \Delta G/G_P$ (where $G_{AP}(G_P)$ are the conductance of the system for antiparallel (AP) and parallel (P) configurations of magnetic moments) can be represented by the expression

$$\frac{\Delta G}{G_P} = \frac{2P_1P_2}{1+P_1P_2}, \tag{2}$$

where P_1 and P_2 are the spin polarization values, depending on the DOS of the charge carriers in the first and the second ferromagnetic electrodes. The relative change in the resistance of the tunneling structure upon reorientation of the magnetization of one of the FM layers is called tunneling magnetoresistance (TMR):

$$\text{TMR} = \frac{R_{AP}-R_P}{R_P} = -\frac{\Delta G}{G_{AP}} = \frac{2P_1P_2}{1-P_1P_2}, \tag{3}$$

where R_P and R_{AP} are the tunnel structure resistances for parallel and antiparallel orientations of the magnetization of the layers, respectively. The interest to the TMR effect increased significantly in 1995, when two scientific groups led by Miyazaki (Fe–Al_2O_3–Fe systems) [12] and Moodera [13] (CoFe–Al_2O_3–NiFe systems) have created samples that show TMR even at room temperatures. In the first experiments, its value was at most 30–50%. Subsequently, Fe–MgO–Fe films were grown, in which the TMR effect at room temperature reached 200% [14, 15] and even 604% [16].

1.4. Tunneling Hamiltonian approximation

An increase in the conductivity of a tunnel contact for parallel orientation of magnetic moments in adjacent ferromagnetic layers has a clear physical explanation, which we present in this section. In the tunneling Hamiltonian approximation [17], that is applicable at low transparency of the barrier, the tunneling conductivity is proportional to the product of the densities of electron states $\rho_{R,L}^{\uparrow\downarrow}(\varepsilon_F)$ in the right (R) and the left (L) electrodes [10]:

$$\sigma = A\left[\rho_R^{\uparrow}(\varepsilon_F)\rho_L^{\uparrow}(\varepsilon_F)+\rho_R^{\downarrow}(\varepsilon_F)\rho_L^{\downarrow}(\varepsilon_F)\right]. \tag{4}$$

For the parallel orientation of the magnetizations in the FM electrodes, assuming that $\rho_L^{\uparrow\downarrow}(\varepsilon_F)=\rho_R^{\uparrow\downarrow}(\varepsilon_F)=\rho^{\uparrow\downarrow}(\varepsilon_F)$, the system conductivity can be written in the following form:

$$\sigma_P = A[\rho^{\uparrow}(\varepsilon_F)\rho^{\uparrow}(\varepsilon_F)+\rho^{\downarrow}(\varepsilon_F)\rho^{\downarrow}(\varepsilon_F)]. \tag{5}$$

For the antiparallel orientation, with the same assumption $\rho_L^{\uparrow\downarrow}(\varepsilon_F)=\rho_R^{\downarrow\uparrow}(\varepsilon_F)=\rho^{\uparrow\downarrow}(\varepsilon_F)$, we get

$$\sigma_{AP} = 2A\rho^{\uparrow}(\varepsilon_F)\rho^{\downarrow}(\varepsilon_F), \tag{6}$$

where A is a constant that exponentially depends on the barrier thickness.

Then the relative magnetoresistance in the Julliere model [11] is

$$\frac{\sigma_P-\sigma_{AP}}{\sigma_P} = \frac{2P^2}{1+P^2}, \tag{7}$$

where P is the spin polarization of electrons in the FM electrode, determined by Eq. (1).

Figure 2 schematically shows a tunnel FIF′ contact. The *d*-electron bands in contacts are split by exchange interaction. When describing the tunnel current flowing through a FIF contact, two spin current channels are usually considered. Let the FM electrodes have the opposite direction of their magnetization in the absence of a magnetic field, as shown in Fig. 2(a). In the antiparallel configuration of contacts magnetization, the tunneling of electrons with spin down from a large number of occupied states to a small number of free states and vice versa is possible. For electrons with spin up, situation is the opposite [Fig. 2(a)].

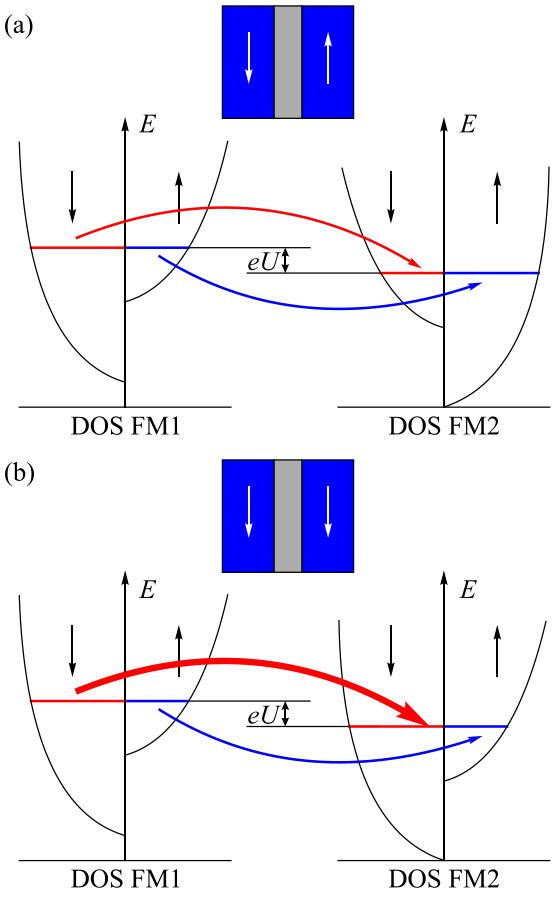

Fig. 2. Spin currents in FIF contact with antiparallel (a) and parallel (b) magnetization.

Turning on the magnetic field results in a parallel orientation of the magnetization of the FM electrodes. The band diagram for this case is shown in Fig. 2(b). For parallel configuration of the contacts magnetizations, electrons with spin up states tunnel from a small number of occupied states to a small number of free ones while the electrons with spin down states from a large number of occupied states to a large number of free ones. Thereby, the FIF structure conductivity with the parallel magnetization of the layers σ_P (5) is always higher than with the antiparallel one σ_{AP} (6).

1.5. Slonchevsky formula

The problem of electron tunneling through a rectangular barrier between two different ferromagnets (F, F′), assuming that their magnetic moments are misoriented by an arbitrary angle θ has been solved in Ref. 18. A quantum-mechanical calculation performed by Slonchevsky within the framework of the free electron model with allowance for exchange splitting led to the following result:

$$\frac{G_P - G_\theta}{G_P} = \frac{2P_{1b}P_{2b}\sin^2(\theta/2)}{1+P_{1b}P_{2b}} \tag{8}$$

in which the spin polarization coefficients have the form

$$P_{1b,2b} = P_{1,2}\frac{\chi^2 - k_{1,2}^{\uparrow}k_{1,2}^{\downarrow}}{\chi^2 + k_{1,2}^{\uparrow}k_{1,2}^{\downarrow}}. \tag{9}$$

Here G_θ is the system conductance at a misorientation of the magnetic moments by an arbitrary angle θ; $P_{1,2}$ are the spin polarizations in the FM electrodes; $k_{1,2}^{\uparrow}(\varepsilon_F)$, $k_{1,2}^{\downarrow}(\varepsilon_F)$ are the wave vectors of an electron with Fermi energy and spin (↑↓) for each of two ferromagnets; $i\chi$ is the imaginary wave vector of the electron corresponding to the inverse length of the exponential decay of the electron wave function inside the barrier. The appearance of an additional factor in formula (9) is a consequence of taking into account the dependence of the tunneling probability on the wave vectors $k_{1,2}^{\uparrow\downarrow}(\varepsilon_F)$.

In addition to the direct electron tunneling through the dielectric barrier considered in the Ref. 18, there are other, more complex mechanisms for the passage of electrons through the classically forbidden area. These may be resonant tunneling through localized states, inelastic tunneling by a transition from one localized state to another, etc. The ratio of different tunneling mechanisms is influenced not only by the material of the dielectric layer, the intrinsic bulk properties of the ferromagnet, and the degree of its spin polarization, but also by the quality of the interfaces. The TMR value can also depend on the properties of the material near the interface (or even on the FM metal-dielectric interface itself) with a thickness of several atomic layers, through which the tunneling process is going on [12].

2. Half-metals

2.1. Half-metals as a special class of ferromagnets

Of particular interest for practical application in spintronics are the so-called half-metals, in which the spin polarization magnitude is not limited and, from a theoretical standpoint, may reach 100% with decreasing temperature. The term “half-metals” should not be confused with the term “semimetals”, which refers to nonmagnetic metals such as Bi or Sb with a low concentration of charge carriers.

Half-metals constitute a separate class of FM materials that have electrons only with spin up or spin down states at the Fermi level. The terms “spin up” (↑) and “spin down” (↓) usually mean orthogonal spin states responsible for the Zeeman effect, i.e., spin states collinear and anticollinear to an external magnetic field or a magnetization vector.

Ferromagnetic elements of the periodic table are not half-metals. Such metals have the values of spin polarization P that never exceed 50%. For example, even at the lowest temperatures for Fe $P = 40\%$, for Co $P = 35\%$ and for Ni $P = 23\%$ [19]. This is due to the fact that the Fermi level in these materials is also crossed by the nonpolarized *s* zone. Consequently, even at the lowest temperatures, a finite density of states at the Fermi level is retained for electrons with both upward and downward spin directions. To obtain only spin up (↑) or only spin down (↓) electrons at the Fermi level it is necessary to change the position of the 3*d* or 4*s* bands by hybridization, going from a pure element to an alloy or a compound. Thus, only systems containing more than one element may become half-metals. Most of the currently known half-metals are oxides, sulfides, or Heusler alloys — ternary intermetallic compounds with a cubic fcc lattice and a chemical formula X_2YZ. Here X and Y are symbols for transition metals, and Z is a heavy *p* element such as Sb, which tends to reduce the energy of 3*d*-level electrons below the edge of the 4*s* band due to *p*–*d* hybridization. All half-metals have a spin gap $\Delta_\uparrow$ or $\Delta_\downarrow$ and a narrower gap Δ_{sf} for spin-flip excitations (see Fig. 3) at the E_F level (such as spin waves).

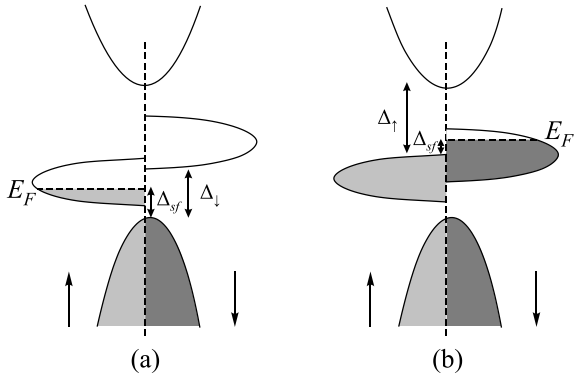

Fig. 3. Schemes for the density of states in half-metals [20]: (a) type I_A for only spin up (↑) electrons at E_F level, (b) type I_B for only spin down (↓) electrons at E_F. Type II is for the case when current carriers at the E_F level are localized in narrow *d* bands

2.2. Classification of half-metals

According to the classification presented in [20], half-metals are divided into four classes, each of which has two subgroups corresponding to spin directions. Half-metals of the first class include metal oxides, in which unpolarized 4*s* states are shifted in energy above the E_F level due to hybridization with 2*p* oxygen states. These are type I_A half-metals if they have less than five *d* electrons [Fig. 3(a)], or type I_B half-metals if they have more than five *d* electrons [Fig. 3(b)]. Type I_A half-metals include, in particular, CrO_2, in which spin up electrons of chromium at E_F are in t_{2g} (↑) state [21]. Another example of a type I_A half-metal is a half-Heusler alloy NiMnSb, in which Ni electrons are at the Fermi level in e_g (↑) state [22].

Type I_B half-metals includes, for example, Sr_2FeMoO_6 oxide, in which t_{2g} (↓) molybdenum conduction electrons at the Fermi level are in spin down state [23]. Another example of a type I_B half-metal is Heusler alloy Mn_2VAl with t_{2g} (↓) manganese electrons at the E_F level [24].

The second type includes half-metals, in which electrons in one of the spin states turn out to be localized in a narrow *d* band. These may be either heavy carriers that form polarons (in this case, conduction will be performed by hopping from one site to another without changing the spin direction), or the states at the edge of the conduction band may be localized due to disorder (then there is a mobility edge for the charge carriers and conduction in one of the spin channels will be realized due to excitations with energies above this edge). In both cases, there must be an activation type of resistance behavior $\rho \approx \rho_\infty \exp(E_a / kT)$ in one of the spin channels with an activation energy $E_a \approx 0.1$ eV, and with a decrease in temperature this channel may be completely localized. A well-known example of a type II_B half-metal is magnetite $FeO{\cdot}Fe_2O_3$ (with gross formula Fe_3O_4), in which the t_{2g} (↓) electrons of Fe jump between the B-sites of the spinel structure, located in the octahedral environment of oxygen atoms, and become localized with decreasing temperature [25].

Half-metals of the third class are known as "transport half-metals". For such metals, there is a nonzero density of states for both spin directions at the Fermi level, but the carriers in one of the spin states have an effective mass much larger than the carriers with the opposite spin state. Therefore, only one type of carriers makes a significant contribution to the conductivity. An example of a type III_A half-metal [Fig. 4(a)] is optimally doped manganite $La_{0.7}Sr_{0.3}MnO_3$, in which highly mobile e_g (↑) Mn electrons and low-mobile t_{2g} (↓) Mn electrons coexist at the Fermi level E_F. Heavy Mn carriers in t_{2g} (↓) state do contribute to the activation

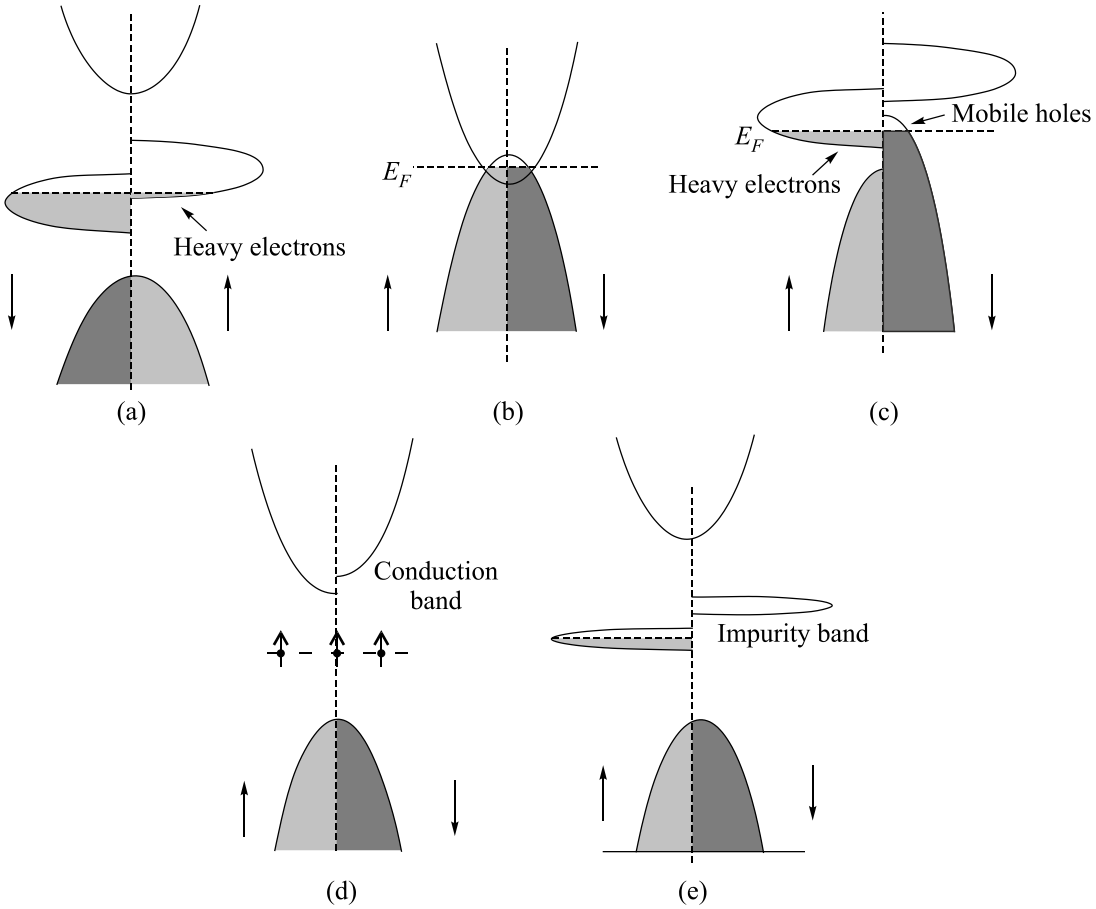

Fig. 4. Densities of states [20] for: (a) type III_A half-metals, in which electrons with one of the spin polarization are mobile and with the other one are localized, (b) magnetic semimetals, (c) type IV_A half-metals, and (d), (e) two types of ferromagnetic semiconductors.

resistance behavior $\rho \approx \rho_\infty \exp(E_a / kT)$, but it is shunted by the metallic type resistance of light e_g (↑) Mn carriers $\rho \approx \rho_0 + \rho(T)$, where ρ_0 is a small residual resistance [26].

As mentioned earlier, a distinction should be made between half-metals and semimetals. Semimetals (the classic examples of which are Bi and Sb) are usually nonmagnetic and have a small but equal number of electrons and holes (≈ 0.01 per atom) due to the occasional small overlap of their valence and conduction bands [see Fig. 4(b)]. However, if a semimetal is magnetically ordered and has a large difference in the effective masses of electrons and holes, it can be classified as a type IV half-metal. An example of such a half-metal is $Tl_2Mn_2O_7$ [Fig. 4(c)]. This material has a small amount of heavy (↑) holes in the ceiling of the e_g zone of manganese, and at the same time there is an equal number of light (↓) 6*s* electrons of thallium [27].

Some ferromagnetic semiconductors can also turn out to be half-metals [Figs. 4(d) and 4(e)] due to the peculiarities of their electronic structure. For example, if their localized ionic cores happen to be able to polarize the conduction or valence band by *S*·*s* exchange, creating a spin splitting that exceeds the Fermi energy. This case includes EuO and EuS doped with trivalent rare-earth ions R^{3+} and a half-Heusler alloy (GaMn)As. Another possibility may arise if the impurity atoms are lying close enough to each other and form a narrow band, which is unstable with respect to spin splitting. In this case, half-metals may not contain any magnetic atoms at all. Hypothetically, $(La_{0.005}Ca_{0.995})B_6$ belongs to this category [28].

The given classification shows that CrO_2 is one of few oxides that can be unambiguously classified as ideal half-metal. Andreev reflection experiments confirmed the spin polarization of CrO_2 films at low temperatures up to 95% [29]. The practical interest in studying materials with almost 100% spin polarization is caused by the possibility of a creation of high-efficiency spintronic devices. One of the main criteria for implementing such devices is the high value of the tunneling magnetoresistance in low magnetic fields.

3. Chromium dioxide as a type I_A half-metal

CrO_2 is the only binary oxide that is a spin-polarized ferromagnetic metal. It is the simplest and most studied half-metal. Chromium dioxide has a rutile-type crystal structure with space group $P4_2/mnm$ [30] with a tetragonal Bravais lattice (Fig. 5) with two formula units per unit cell. It consists of Cr atoms surrounded by oxygen octahedra. Oxygen octahedra are orthorhombically distorted relative to the ideal geometry. The apical oxygen atoms have a slightly greater distance from the central chromium atom than the equatorial ones. It is assumed that these distortions are due to the Jahn–Teller effect [31]. Chromium atoms are localized in positions [0, 0, 0] and [½, ½, ½] in lattice coordinates while four oxygen atoms are localized at [*u*, *u*, 0], [1 – *u*, 1 – *u*, 0], [½ + *u*, ½ – *u*, ½] and [½ – *u*, ½ + *u*, ½], where *u* is the magnitude of the shift relative to the internal coordinates of

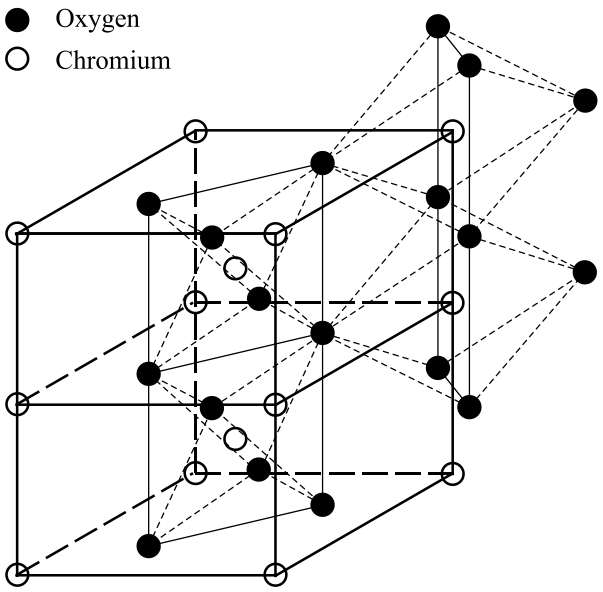

Fig. 5. Crystal structure of CrO_2 rutile type [21]. Bold solid and dashed lines mark the unit cell. The thin lines mark the oxygen octahedra surrounding each chromium atom. Solid thin lines in the octahedra highlight the equatorial planes, and the dotted lines connect these planes with the apical (vertex) oxygen atoms.

the unit cell. The measured values of the structural parameters are: $a = 4.419$ Å, $c = 2.912$ Å and the dimensionless parameter $u = 0.303$ [21]. The electronic configuration of CrO_2 is represented by the states $t_{2g}{}^2\uparrow$ for ions Cr^{4+} and $2p^6$ for O^{2-}. There is a small charge transfer from oxygen to chromium: $O^{2-} \rightarrow Cr^{4+}$ and strong mixing of oxygen holes and chromium electronic states at the Fermi level E_F. The calculation of the band structure, carried out in the local spin density approximation (LSDA+*U* method), showed that CrO_2 could be considered as a "self-doped ferromagnet". This explains why, despite the narrowness of the *d* bands and the large value of the obtained Coulomb correction *U*, chromium dioxide is a metal but not a Mott insulator [32].

Figure 6 shows the calculated density of states (DOS) of chromium dioxide for the electrons in two spin states: spin up (positive projection on *y* axis) and spin down (negative projection on *y* axis). As seen from Fig. 6, the Fermi level crosses the energy bands of electrons with upward spins (↑) near the local minimum of DOS and lies in the middle of the gap for electrons with downward spins (↓). So, in calculations in the local spin density approximation (LSDA), CrO_2 is a half-metal, as was first shown in Ref. 33. Calculations give a total magnetic moment equal to $2\mu_B/CrO_2$. This result agrees with the experimental value per formula unit obtained from measurements of the saturation magnetization of CrO_2. It is almost completely determined by the contribution of spins of the chromium ions. The calculated orbital contribution is only a few percent [21]. The density of states at the Fermi level with upward spins is 0.69 states/eV/CrO_2. In Fig. 6, a narrow zone located at about 17 eV corresponds to the 2*s* states of oxygen.

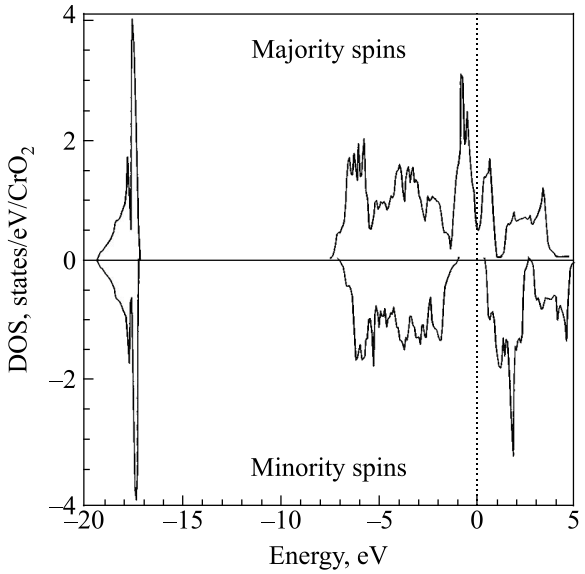

Fig. 6. Density of states in CrO_2. The dotted line marks the Fermi energy E_F [21].

It is identical for both spin directions, lies substantially below the Fermi level in energy and, therefore, does not contribute to the total spin density. The nonzero spin density arises due to the splitting of wide bands by the exchange interaction by approximately 1.7 eV near the Fermi level. These bands mainly include the 3*d* states of chromium in the t_{2g} configuration, while the states of chromium in the e_g configuration are located higher in energy (by about 2.5 eV) due to the splitting by the crystal field (see Fig. 7).

Exchange interaction splits the spins down *d* band at the Fermi level. As a result, t_{2g} spin up zone is filled at 2/3, and the Fermi level is in the middle of the pseudogap for $t_{2g}\uparrow$ states of chromium.

Contour plots of the spin density $s(\mathbf{r}) = n_\uparrow(\mathbf{r}) - n_\downarrow(\mathbf{r})$ are shown in Fig. 8 for two crystal cross-sections. Figure 8(a) shows the plane $(1\bar{1}0)$ formed by the equatorial O atoms and one atom of Cr. Figure 8(b) shows the perpendicular plane including two equatorial and two apical O atoms. Related contour levels are separated by 0.3 μ_B per formula unit. Areas of zero density are designated by dotted lines. The positions of the Cr and O atoms are designated by squares and circles, respectively. Apical and equatorial O atoms are indicated by indices. Figure 8 shows that the spin density is strongly localized near the Cr atoms and is determined almost exclusively by the 3*d*

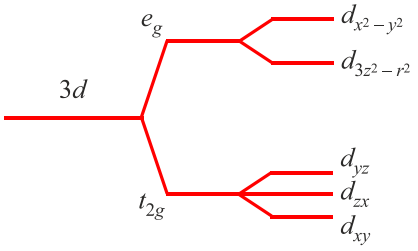

Fig. 7. Splitting of 3*d* states of Cr.

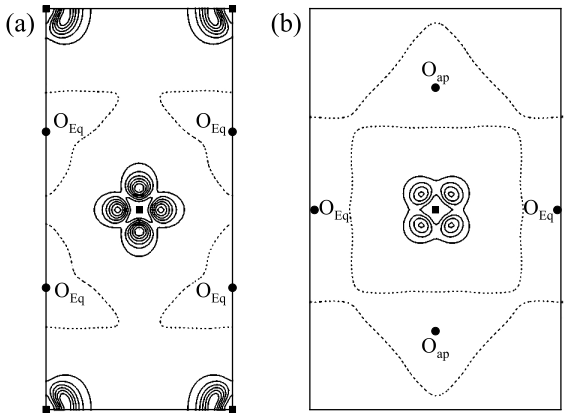

Fig. 8. Spin density of CrO_2: (a) in equatorial plane of oxygen octahedra, (b) in the plane of octahedra containing two equatorial and two apical oxygen atoms [21].

states of Cr. Figure 8(a) shows that the spin density distribution has the shape of a "clover leaf" for the d_{xy} function. Here, a local coordinate system is used with the origin on the chromium atom and the *x*, *y*, and *z* axes directed towards the octahedral oxygen atoms. Apical oxygen defines the local *z* axis. It is well known that the crystal field created by the octahedron of negative charges surrounding the *d*-metal atom splits the *d* states of transition metal ions into three t_{2g} states (d_{xy}, d_{yz}, d_{zx}), which have lower energy, and two e_g states ($d_{x^2} - d_{y^2}$ and $d_{3z^2-r^2}$), which have higher energy and do not make a noticeable contribution to the total spin density in CrO_2 (Fig. 7). Figure 8(b) shows the spin density values d_{xz} and d_{yz} for the planes of the unit cell *XZ* and *YZ*, respectively. Spin distribution density d_{xz} is approximately ½ of d_{yz} density.

4. Magnetic properties of CrO_2

The magneto-optical anisotropy of CrO_2 (Kerr effect) calculated from first principles for uniaxial single crystals and polycrystals consisting of uniaxial crystallites is considered in detail in [34]. It is associated with the noncollinearity of the vectors of the magnetization and the orbital magnetic moment.

According to the literature data, the Curie temperature for chromium dioxide is in the range T_C = 392–396 K [20]. At low temperatures, specific magnetization 133 А·м^2/kg (measured at B = 0.824 T) corresponds to the total magnetic moment of 2.0 μ_B/f.u., which is expected for half-metals [35]. There is information in the literature that, in reality, the magnetic moment of chromium dioxide is closer to 2.1 μ_B. However, there is a compensating moment of oxygen 0.05 μ_B/f.u. Such compensation is a consequence of the covalent bond (mixing) between t_{2g} states of chromium and 2*p* states of oxygen [36].

The temperature dependence of magnetization significantly below the Curie temperature T_C obeys Bloch law $T^{3/2}$ [37]:

$$M(T) = M(0)(1 - BT^{3/2}), \qquad (10)$$

where $B = 3.4 \cdot 10^{-5}$ K$^{-3/2}$. The spin-waves stiffness constant D, estimated from the value of the parameter B [37], is approximately 150 meV·Å^2, which indicates the excitation of ferromagnetic spin waves. Spin-wave excitations were also registered in ferromagnetic resonance experiments in thin films [38]. In this study, the estimated value of the spin-wave stiffness constant was $D \approx 70$ meV·Å^2.

The value of magnetocrystalline anisotropy with an easy magnetization axis c, inherent to epitaxial CrO_2 films grown on the (100) plane of a TiO_2 substrate measured at room temperature, is $K_1 = 2.7 \cdot 10^4$ J/m^3 according to the data [39], while, according to another source, it varies with temperature from $K_1 = 6.5 \cdot 10^4$ J/m^3 at $T = 5$ K to $K_1 = 3.7 \cdot 10^4$ J/m^3 at $T = 300$ K [36].

5. Resistive properties of CrO_2

The value of the specific residual resistance of CrO_2, measured on single-crystal samples or high-quality films, has the order of magnitude $\rho_0 \approx 4 \cdot 10^{-8}$ Ω·m [20, 21, 35, 37, 40–42], and the resistivity ratio $\rho(300\text{ K})/\rho_0$ reaches 140 [43]. Below $T = 50$ K CrO_2 behaves like a reasonably good metal with a resistivity being weakly dependent on temperature (Figs. 9, 10).

For the CrO_2 sample with residual resistivity $\rho_0 = 4 \cdot 10^{-8}$ Ω·m the electron mean free path at temperature $T = 5$ K is $\ell \approx 70$ nm [21]. At low temperatures, the functional dependence $\rho(T)$ is well described by the Bloch–Gruneisen law (Fig. 9) and at $T \le 30$ K the $\rho(T)$ approaches the residual resistance ρ_0. Above the Curie temperature, the slope $d\rho/dT$ changes. In this case, the value of resistivity $\rho = 6 \cdot 10^{-6}$ Ω·m is achieved that corresponds to a mean free path $\ell \approx 0.7$ nm, which is pertinent to "bad" metals. Therefore, at temperatures above T_C, CrO_2 can be called a metal only in the sense that $d\rho/dT > 0$. Assuming that the spin splitting persists even above T_C, the mean free path will be $\ell \approx 0.2$ nm, which is slightly larger than the interatomic distance.

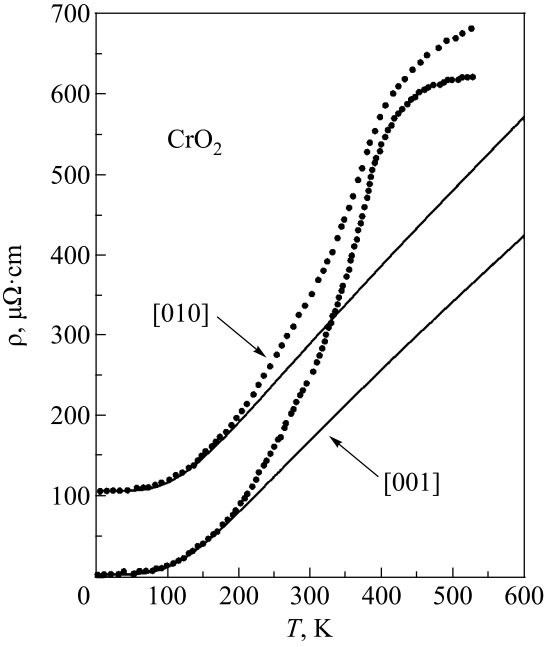

Fig. 9. Temperature dependences of resistivity for CrO_2 single-crystal [21]. The data for [010] direction is shifted upwards by 100 μΩ·cm to avoid overlap. Solid curves are the fitting to the Bloch–Gruneisen function.

The temperature dependence of the resistance for epitaxial CrO_2 (100) films deposited on a TiO_2 (100) substrate was studied experimentally in [42]. At low temperatures ($T \le 40$ K), the dependence $\rho(T) \cong \rho_0 + AT^{\alpha}$ observed, where $\alpha \approx 3$.

The theory [44] predicts that in ordinary itinerant ferromagnets at low temperatures, $\rho(T) \propto T^2$ dependence should be observed due to the one-magnon scattering processes. However, for ideal half-metals, one-magnon spin-flip scattering processes in the ground state are forbidden. Also, another low-temperature dependence $\rho(T) \propto T^{4.5}$ predicted in [45] on the assumption of the rigid-band model for two-magnon processes does not agree with the experiment. The authors of [42] considering spin fluctuations, suggested that one-magnon scattering processes can nevertheless take place in half-metals. In this case, within the framework of the "soft zone" model, they managed to get the $\rho(T) \propto T^3$ dependence, which agrees well with the experimental data for $T < 40$ K.

The authors of the theoretical work [46] obtained the dependence $\rho(T) \propto T^{2.5}$ [for the case of one-magnon scattering in an "almost semimetallic ferromagnet", assuming that the spin down (↓) electrons at the Fermi level near the band edge are in the state of Anderson localization due to strong disorder]. Such dependence indeed has been observed experimentally in [41] (see Fig. 10).

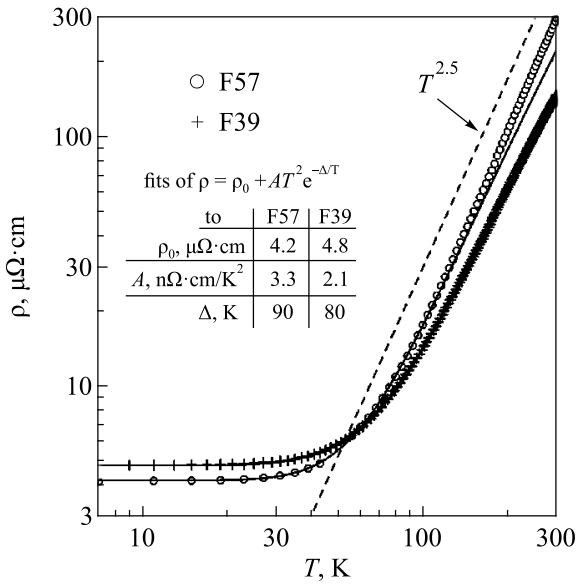

Fig. 10. An example of the temperature dependences of resistivity for two thin textured CrO_2 films [41].

The autors of [37] used the phenomenological expression $\rho(T) \cong \rho_0 + AT^2 \exp(-\Delta/T)$ with $\Delta \approx 80$ K to fit the temperature dependence of the resistance of epitaxial CrO_2 films grown by thermal decomposition of CrO_3 under high pressure. It turned out that this approximation is applicable for epitaxial CrO_2 films in a wide temperature range.

The authors of [41] tried to substantiate it, noting that the $\propto T^2$ dependence may be associated with electron-electron or electron-magnon scattering while the exponential factor can be explained by the presence of a gap in the spectrum of spin excitations for spin-flip processes. However, the experimentally obtained gap width $\Delta \approx 80$ K is too small to be related with both the half-metallic energy gap for the electrons in spin down state (≈ 1.7 eV) and even with the value Δ_{sf} (where $\Delta_{sf} \approx 0.3$ eV is the characteristic energy for spin-flip processes) [20]. Thus, a unified approach to explain the temperature dependences of resistance in epitaxial chromium dioxide films has not yet been developed.

The Hall resistance in CrO_2 may be represented by the sum of the normal and the anomalous terms: $\rho_H = R_0 B + R_S \mu_0 M$. According to [41], the anomalous term reflects the behavior of the magnetization and prevails for $T > 150$ K. The authors believe that the functional dependence $R_S \propto T^4$, which is fulfilled in the temperature range 40–300 K indicates a side-jump mechanism (in this case, dependence $R_S \propto \rho^2$ should appear while $\rho \propto T^4$ for the high-temperature region). The term corresponding to the normal Hall effect dominates in low-temperature range at $T < 80$ K [41].

An interesting feature is a change in the slope of the Hall constant dR_0/dH from positive to negative with increasing magnetic field and the transition to negative values of R_0 with decreasing temperature. If one try to interpret this behavior within the framework of a simple two-band model, then the positive slope of $R_0(H)$ at low temperatures reflects the predominance of highly mobile holes in weak magnetic fields. When switching to a strong field mode $\mu B_c = \omega_c \tau > 1$ in a magnetic field above the critical one, where μ is the mobility, the negative slope $R_0(H)$ shows that less mobile, but prevailing in quantity electrons ($n = 0.4$ electrons / Cr) predominate in the Hall effect. The two-band analysis gives the values $\mu_p \approx 0.25\ T^{-1}$ and $\mu_e \approx 0.01\ T^{-1}$ for hole and electron mobility, respectively. Both holes and electron mobilities have the same temperature dependence: $\mu(0)/\mu(T) = 1 + AT^2 e^{-\Delta/T}$, where $\Delta = 80$ K [41]. The authors note that their analysis using the two-band model is a simplified consideration without taking into account the complex Fermi surface [48]. However, in any case, an essential feature of CrO_2 is mobile $2p$ oxygen holes and heavy t_{2g} electrons (and holes) of chromium.

6. Magnetoresistive properties of CrO_2

The change in the conduction mode with decreasing temperature is also clearly manifested in magnetoresistance behavior [41, 42]. The best media for observing the conducting properties of chromium dioxide are unstressed epitaxial films with low residual resistivity. For such films, the magnetoresistance at $T > 300$ K is negative, isotropic, linearly dependent on temperature, almost independent of the quality of the crystal (film), and its value is less than 1% [49]. This MR is associated with a decrease in the scattering rate due to spin disorder with an increase in the magnetization induced by an external magnetic field. It significantly depends on the substrate material, quality, and orientation; actually, on the density of defects. At low temperatures, a positive perpendicular MR (when the field is perpendicular to the film) and longitudinal MR (when the field is parallel to the film) both change proportionally to B^2. This dependence is a consequence of the high mobility and long mean free path of charge carriers [49].

The extrinsic magnetoresistance in powder compacts is determined by the total influence of the classical magnetoresistance inside of the crystallite material and by the contact and tunneling magnetoresistances between crystallites.

Due to the difficulty of obtaining high-quality single crystals, the magnetoresistive properties of CrO_2 are most fully studied on epitaxial and polycrystalline films. In [42], CrO_2 films with a Curie temperature of 390–395 K, epitaxially grown on single-crystal TiO_2 substrates with (100) orientation, were studied. The films had magnetic anisotropy in the *bc* plane.

Figure 11 shows the dependences of the resistance of CrO_2 films at $T = 5$ and 380 K on the magnetic field with longitudinal and transverse orientation relative to the film plane. At $T = 5$ K, the magnetoresistance in the transverse direction is positive, proportional to H^2, and reaches 25%, that is, about 6%/T. In longitudinal geometry, low-temperature magnetoresistance is about 0.5%/T. At $T = 380$ K, the negative MR is 1.75%/T regardless of the field orientation.

The positive magnetoresistance at low temperatures is associated with the effect of the Lorentz force acting on electrons inside crystallites. It is usually observed in sufficiently pure metals at low temperatures. The negative MR at high temperatures is explained by the suppression of the spin disorder by the external magnetic field, which reaches its maximum near the T_C.

The magnetoresistance of textured CrO_2 films, obtained by chemical deposition on ZrO_2 substrate, was studied in [50, 51]. The measurements were carried out by the four-contact method with an electrical current directed parallel to the crystallographic plane (100). The paper [50] published in 1998 partially confirmed the $\rho(T)$ data obtained by Rodbell and DeVries in 1966 for the CrO_2 single crystal [40]. Also, the longitudinal and transverse magnetoresistance of the film deposited on the ZrO_2 substrate was measured. The film thickness was 0.80 μm. The measurements were carried out in the temperature range 0.55–380 K in magnetic fields up to 10 T. For both orientations of the magnetic field, the MR turned out to be negative and linearly dependent on the field at $T > 200$ K in magnetic fields up to $B = 3$ T [Fig. 12(a)].

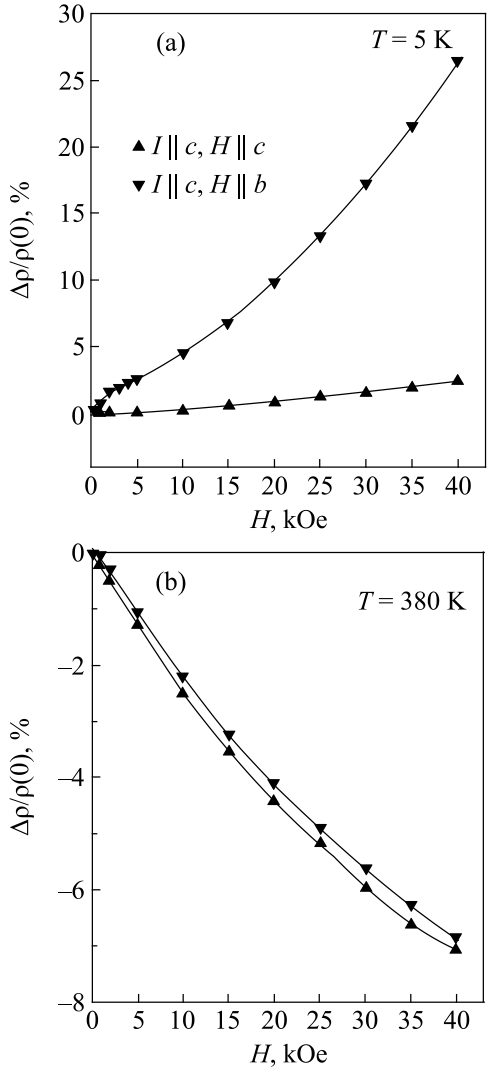

Fig. 11. Longitudinal ($H \| c$) and transverse ($H \| b$) magnetoresistance (0–40 kOe) of epitaxial chromium dioxide films with a thickness 4000 Å, measured at $T = 5$ (a) and 380 K (b). In both cases, the current was directed along the easy magnetization axis c [42].

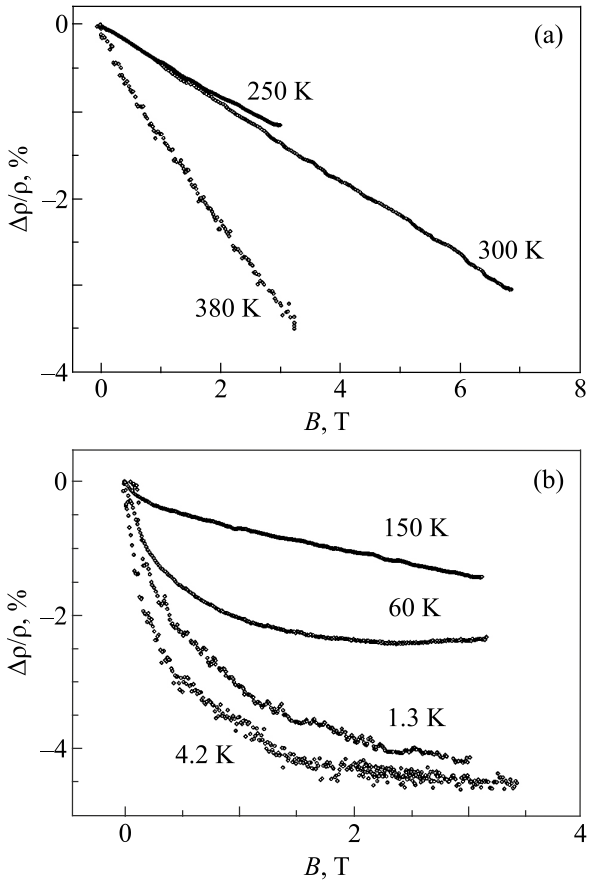

Fig. 12. Longitudinal MR for high (a) and low (b) temperatures [50].

The value of the longitudinal negative magnetoresistance decreased with decreasing temperature to 200 K, but for $T < 200$ K the magnetoresistance began to increase, demonstrating a nonlinear dependence [Fig. 12(b)] on the magnetic field up to 3.5 T. The maximum values of negative magnetoresistance were 1.4%/T at $T = 380$ K and 4.3%/T at $T = 4.2$ K.

Figure 13(a) shows that the temperature dependence of the longitudinal magnetoresistance measured in a magnetic field of $B = 2.93$ T has a minimum at $T \sim 200$ K and a noticeable increase at $T > 300$ K, apparently due to an increase in spin fluctuations when approaching the $T_C = 390$ K, as might be expected from the interpretation of CrO_2 as a self-doped double exchange ferromagnet [52].

Figure 13(b) demonstrates that the longitudinal negative magnetoresistance increases with decreasing temperature, but at $T < 5$ K it starts to decrease again. In this temperature range, resistivity measurements indicate the absence of magnon excitations and/or spin fluctuations. Such a decrease in the magnetoresistance magnitude for $T < 5$ K is, possibly, related to the effect of a decrease in spin-flip scattering, as in the case of the semimetallic ferromagnet $La_{1-x}Sr_xMnO_3$ ($x = 0.175$, 0.2) [53].

Figures 14 show the magnetic field dependence of the transverse magnetoresistance in the case when the magnetic field was perpendicular to the current and the film plane, in the high-temperature and low-temperature regions. It turned out that at high temperatures the field and temperature dependences of the transverse magnetoresistance are similar to those in the longitudinal field. However, at low temperatures, the behavior of the magnetoresistance in a transverse magnetic field has a complex temperature dependence in low fields [Fig. 14(b)]. In the region of higher fields and low temperatures, the value of negative magnetoresistance decreases with increasing field, following the B^2 dependence, inherent to the cyclotron orbital motion of conduction electrons.

The dependence of the longitudinal magnetoresistance of CrO_2 films on the crystallites orientation and a small change in the angle between the applied field and the substrates plane was studied in [51] at $T = 1.3$ K. The authors compared the magnetoresistance of CrO_2 films deposited

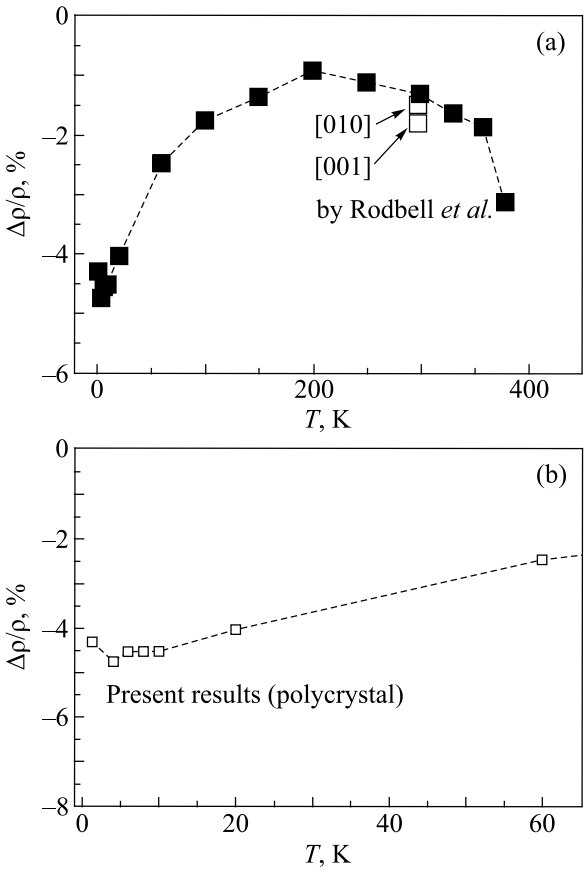

Fig. 13. High-temperature (a) and low-temperature (b) dependences of longitudinal magnetoresistance of a textured CrO_2 film on a ZrO_2 substrate at $B = 2.93$ T [50].

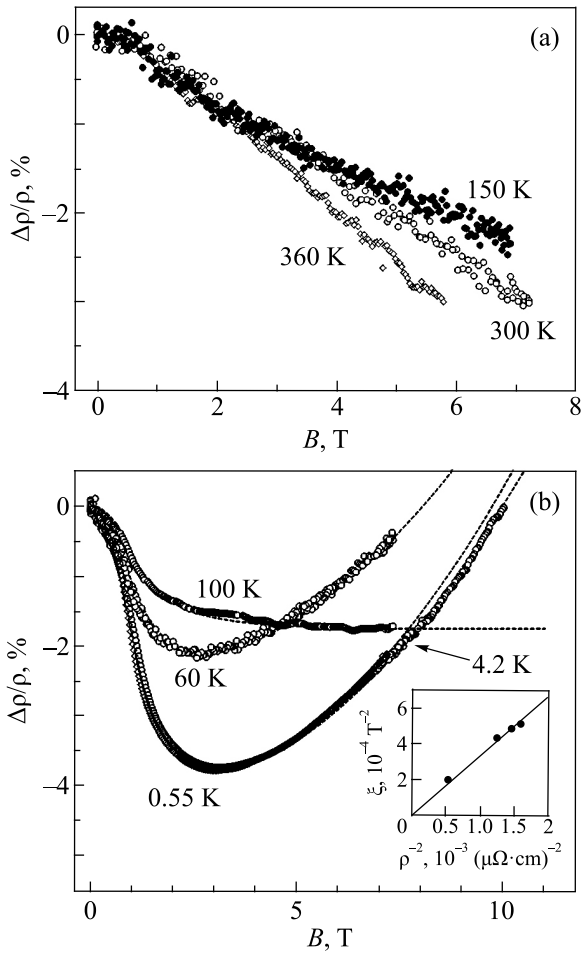

Fig. 14. Transverse magnetoresistance of CrO_2 film at high (a) and low (b) temperatures. The dotted lines are the result of computer simulation. The inset shows the relative contribution of the cyclotron orbital motion effect as a function of the inverse square of resistivity [50].

on a ZrO_2 substrate (in this case, the films grown with a texture of ⟨100⟩ in the direction perpendicular to the plane of the substrate) and the magnetoresistance of CrO_2 films deposited on a TiO_2/Si (111) substrate. Films grown on a TiO_2/Si (111) substrate have a mixed texture with crystallite orientations ⟨100⟩ and ⟨110⟩ directed perpendicular to the plane of the substrate with a predominated orientation ⟨100⟩. The samples studied were deposited under the same conditions, had an equal thickness and good electrical contacts between crystallites, as evidenced by the close temperature dependences of their resistance. Nevertheless, the amplitude of the transverse magnetoresistance turned out to be twice large for the films with the mixed orientations of crystallites ⟨100⟩ and ⟨110⟩ on a TiO_2/Si (111) substrate as compared with the films of the same thickness and composition, but with a strict orientation of ⟨100⟩, grown on a ZrO_2 substrate.

Also, the authors [51] showed that changing the substrate orientation by a small angle $\alpha = 10°$ relative to the direction of the field causes a decrease in the magnitude of the longitudinal magnetoresistance by 25% in a magnetic field $B = 3$ T (Fig. 15).

Since the effect of changing the cyclotron orbital motion of electrons should be small at these angles, a twofold increase in magnetoresistance and its strong angular

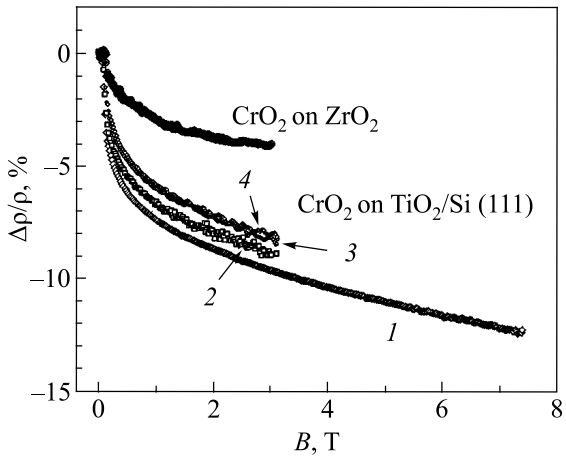

Fig. 15. Longitudinal magnetoresistance of CrO_2 film grown on a TiO_2/Si (111) substrate at $T = 1.3$ K depending on the substrate inclination angle. Curves *1*, *3*, and *4* correspond to the slopes of the substrate 0°, +10°, and –10° relative to the applied fields direction. Curve *2* is the result for the tilting angles ±5°. Upper curve shows for comparison the data for textured CrO_2 (100) film deposited on the ZrO_2 substrate [51].

dependence, compared to a CrO_2 film having only one texture orientation ⟨100⟩, means the dominant influence of the crystallite orientation on the magnetoresistance value.

The maximum magnetoresistance value was obtained for the field orientation along the film plane (100), and was approximately 1.7%/T at $T = 1.30$ K [51].

Similar results were shown by measurements of powder composites in which the magnetic texture associated with the shape anisotropy of needle-shaped CrO_2 nanoparticles arose due to uniaxial compression [54]. A change in the magnetic field direction by 90° towards the texture of needle-shaped crystallites lying in the pressing plane led to a change in the magnetoresistance from 36% to 28%. The observed effect was associated with the difference in the magnetic susceptibility when an external magnetic field was applied in the direction of the easy magnetization axis (approximately coinciding with the longitudinal axis of the needle-shaped nanoparticles) and perpendicular to this axis [55].

In [56], the influence of the configuration of magnetic domains on the magnetoresistance of narrow (0.5–5 μm wide) epitaxial CrO_2 (100) wires grown on a TiO_2 (100) substrate and oriented along different crystallographic directions was studied. The configuration of the magnetization for different orientations of the film was studied using a magnetic force microscope. The authors were able to observe the formation of a single-domain state in the case of a ease magnetic structure (when the film is oriented along the easy magnetization axis) and the formation of a stripe domain configuration for the films oriented along the hard magnetization axis. To study the interrelation between various contributions to film anisotropy, the authors studied magnetization reversal processes in CrO_2 films, when their length significantly exceeded their width, by measuring the magnetoresistance for different magnetic field orientations relative to the easy and hard magnetization axes. Figure 16 demonstrates the dependences of resistance on the magnetic field at $T = 4.2$ K for the film of 2 μm wide oriented along the easy axis. The magnetic field was applied both parallel [Fig. 16(a)] and perpendicular [Fig. 16(b)] to the ⟨001⟩ direction. Figures 16(c) and (d) show the same dependences at $T = 4.2$ K for the strip of film propagating along the hard magnetic axis. The processes of magnetization reversal for these two structures are noticeably different. The study of the mechanisms of magnetization reversal for different orientations of CrO_2 films to the external magnetic field direction and the directions of magnetocrystalline anisotropy showed that the process of magnetization reversal of epitaxial CrO_2 films is very sensitive to the relationship between the magnetocrystalline anisotropy, the anisotropy of the sample shape, and Zeeman energy of magnetic moments. The diagrams at the top of each graph in Fig. 16 show the different configurations of magnetic domains during magnetization reversal [56].

As a result, the authors showed that the magnetoresistance of the film with magnetocrystalline anisotropy lying in the direction perpendicular to the anisotropy of the sample

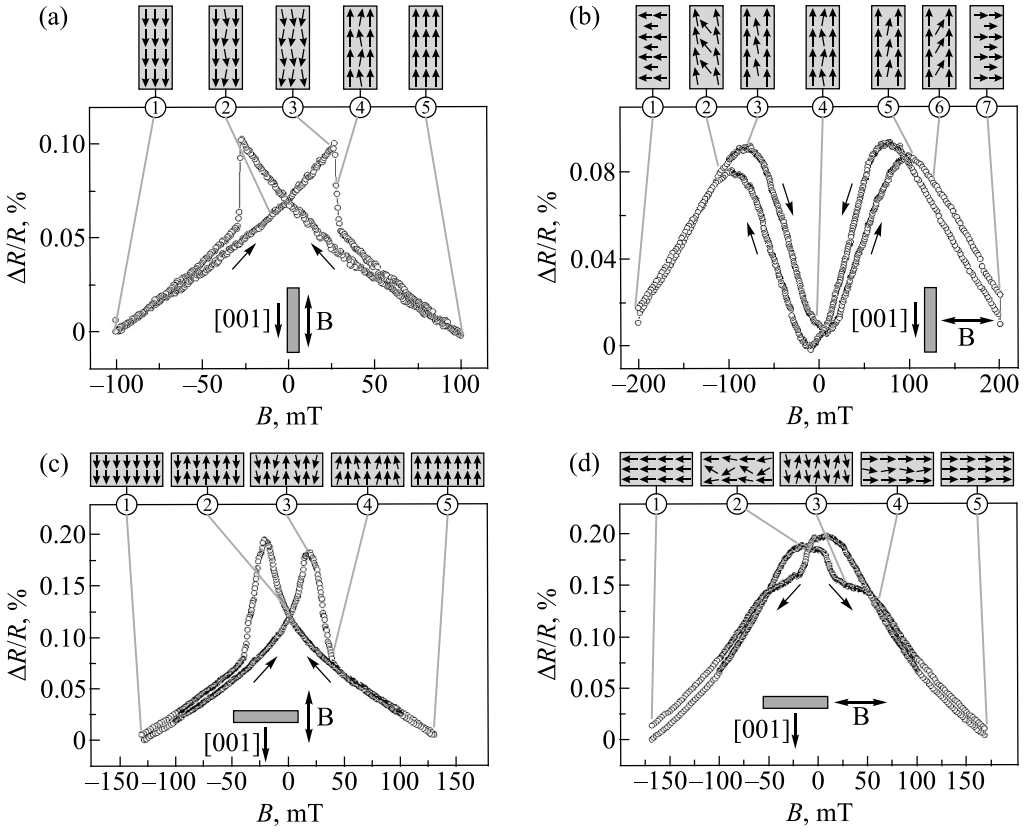

Fig. 16. Field dependences of magnetoresistance of a film 2 μm wide oriented along the easy (a), (b) and hard (c), (d) axes [56].

shape and the direction of the external magnetic field could not be explained without taking into account that the film consists of crystallites, each of which has its easy magnetization axes, slightly inclined relative to the macroscopic easy magnetization axis of the whole sample studied. Also, the measurements of the temperature dependence of the magnetoresistance undertaken by the authors of [56] showed that at low temperatures, the intergrain tunneling magnetoresistance with the value of ≈ 40 %/T prevails in any case while at room temperatures it is replaced by a small anisotropic magnetoresistance with a value of ≈ 1%/T. It is essential to note that at $T = 4.2$ K for a film oriented along the easy axis, as in [41], a positive magnetoresistance has been observed for $B \perp I$ (where I is the measurement current) and B perpendicular to the length of the film sample (Fig. 16). For case $B \parallel I$ and B parallel to the long axis of the film, a positive magnetoresistance was observed in low fields, which changed to a negative one with increasing field. The maximum value of the negative magnetoresistance in the first case reached ~ 0.75 %/T. As for the film oriented along the hard axis, the negative magnetoresistance value reached ~ 0.96%/T for the case $B \parallel (001)$ and 0.1%/T for $B \perp (001)$.

This brief review of the known experimental studies of the transport properties of chromium dioxide shows that at low temperatures CrO_2 possesses a metallic type of conductivity with a small residual resistance inherent to "good" metals. Despite the high spin polarization, pure chromium dioxide by itself has a very low magnetoresistance, which is determined by the values of magnetocrystalline anisotropy, the anisotropy of the sample shape, and the direction of the external magnetic field. Generally, the measured transport properties of chromium dioxide are in good agreement with the calculated band structure.

7. Tunneling magnetoresistance in cooperative systems of magnetic tunnel junctions

As well as the properties of tunnel structures based on FM materials with nearly 100% spin polarization are fundamentally different from the properties of pure half-metals, the high values of magnetoresistance pertinent to the effect of spin-dependent electron tunneling acquire some peculiarities in cooperative systems — systems consisting of a large number of similar magnetic tunnel junctions. One of the advantages of cooperative systems is the ability to enhance spin-dependent electronic effects. Granular magnetic materials, in which thin dielectric layers separate FM granules, are promising materials for studying the phenomena caused by spin-dependent electron transport in cooperative magnetic systems. These interlayers play the role of tunnel barriers, forming an extensive network of magnetic tunnel contacts. The resistance in such a system depends on the magnetizations of neighboring granules near the contact [57].

A theoretical explanation of the magnetoresistive effect associated with intergranular tunneling was given in [58]. The authors applied their theory to explain the features of the magnetotransport properties of the granular Ni film. The used model considers the additional exchange energy arising when the magnetic moments of the neighboring granules are not parallel, while the electron spin is conserved during tunneling between the granules. Taking into account only linear terms in the expansion for the magnetic energy when calculating the exchange interaction constant, they write the expression for the magnetoresistance in the following form:

$$\frac{\Delta\rho}{\rho_0} = -\frac{PJ}{4k_BT}\left[M^2(H,T) - M^2(0,T)\right], \qquad (11)$$

where J is the exchange interaction constant, P is the degree of spin polarization of electrons in neighboring granules separated by a tunnel barrier, M is the magnetization. The proposed model makes it possible to predict both the field and temperature dependences of the TMR value in granular magnetic films as cooperative systems of magnetic tunnel contacts.

The extrinsic transport properties of systems based on chromium dioxide have been experimentally studied in tunnel contacts, polycrystalline films, pressed powders, and point contacts. As an example, consider the CrO_2/dielectric/Co tunnel contact. For FM CrO_2 particles, a natural dielectric barrier can be easily formed during synthesis. It is an antiferromagnetic oxide layer Cr_2O_3 with Néel temperature $T_N = 300$ K and thickness ~ 2–3 nm [60].

Tunnel contacts CrO_2/Al_2O_3/Co demonstrate the negative TMR of ~ 1% at 77 K and ~ 8% at 4.2 K [61]. At the same time, cooperative systems — polycrystalline films [62] and powder compounds (mixtures of CrO_2 and Cr_2O_3 particles) [63–65] — have significantly higher TMR values.

As noted in [59], powder systems in which thin dielectric layers separate FM particles with a metallic type of conductivity are promising materials for studying the phenomena associated with spin-dependent electron transport in cooperative tunnel systems. The resistance of such a system depends on the direction of the magnetization vectors in two neighboring particles. In the ideal case, the tunneling of electrons through a potential barrier between two particles, in which the magnetization axes do not coincide, changes as $\cos^2(\theta_{ij}/2) = 1 + \cos\theta_{ij}$, where θ_{ij} is the angle between directions of magnetic axes. Let the symbol ρ_r denote a powder system resistivity with a completely random distribution of the particle magnetizations (i.e., $\langle\cos\theta_{ij}\rangle = 0$) and $\rho\parallel$ is the resistivity in the strictly parallel orientation of the magnetic moments of granules (i.e., the extrapolated value of the resistance to the field $H \to \infty$). Then the theoretically possible maximum of the TMR is 50% [20]:

$$\mathrm{TMR} = \frac{\left(\sigma_{\parallel} - \sigma_r\right)}{\sigma_{\parallel}} = \frac{\left(\rho_r - \rho_{\parallel}\right)}{\rho_r}. \qquad (12)$$

When passing from paired averaging to averaging over orientation for an arbitrarily chosen ith particle in the sample, where θ_i is the angle between the direction of the magnetic axis of the ith particle and the external magnetic field applied to the sample, the authors [59] get $\left\langle \cos\theta_{ij} \right\rangle = \left\langle \cos\theta_i \right\rangle^2 = m^2$, where $m = (M/M_s)$ is the value of the relative magnetization, M_s is the saturated magnetization. Then, if not all magnetic moments are aligned totally parallel to the field, expression (11) is reduced to the expression $\mathrm{TMR} = m^2/(1 + m^2)$, and for the case of incomplete polarization, the tunneling probability and, accordingly, the TMR value in Julliere model [11] will be equal to $P^2/(1 + P^2)$ [20].

At liquid helium temperatures, the maximum TMR values of 40% were obtained in [66] for a composite powder system based on CrO_2-β-CrOOH (with 1.73 nm thick insulating layer). According to the formula $\mathrm{TMR} = P^2/(1 + P^2)$, the degree of spin polarization reached $P = 82\%$ in this case. In [65], if comparing the maximum resistance value in magnetic fields near the coercive field with the resistance of a completely magnetized powder at $T = 5$ K, a similar TMR value was obtained ≈ 41%. However, the P values determined in this way are overestimated for two reasons. First, in the initial nonmagnetized state, the system resistivity should be higher than in a coercive field. It is known that the disordering of the magnetic moments in the initially prepared sample, which has never been in a magnetic field (so-called "virgin magnetic state"), is always higher than in the state of coercing, where $\left\langle \cos\theta_{ij} \right\rangle > 0$.

Second, there is a nonzero tunneling probability due to spin-wave excitations even in the antiparallel magnetization of electrodes. Thus, measuring the tunnel magnetoresistance cannot serve as a reliable method for determining the degree of spin polarization. In addition, the dependence of TMR on the field H does not always reach saturation even in relatively high magnetic fields ~ 6 T (Fig. 17). More direct

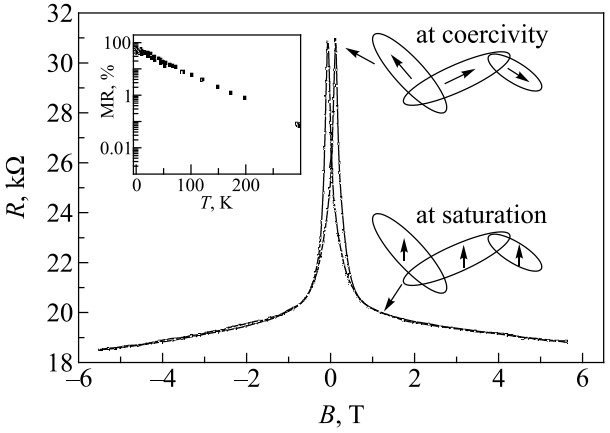

Fig. 17. Magnetoresistance of pressed $CrO_2 - Cr_2O_3$ powder. The inset shows its temperature dependence [59].

methods for measuring spin polarization are spin and angle-resolved photoelectron spectroscopy (SARPES), the study of magneto-optical effects (circularly polarized luminescence in a magnetic field), spin-polarized tunneling microscopy, and Andreev reflection experiments [19, 36]. The highest values of spin polarization obtained in a series of experiments on Andreev reflection at point contacts CrO_2–superconductor [29, 67, 68]. In these experiments at low temperatures, the real values of CrO_2 spin polarization were obtained, which turned out to be equal to $P \approx 80$–96% (at $T = 1$ K).

8. Percolation conductivity of granular half-metal systems

The first works in the field of percolation theory were given up to the processes of infiltration of liquids or gases through a porous medium and to the processes of gel formation [69]. Subsequently, the percolation theory methods were applied to simulate the electrical conductivity in composites, hopping conductivity in semiconductors, etc. At present, the percolation theory is widely used to explain the properties of disordered media at low temperatures. An example of such a medium is a granular system consisting of a mixture of two phases with different conductivity. The particles size can range from a few nanometers to hundreds of nanometers. In particular, a granular system can be a system in which ferromagnetic particles (granules) are in a dielectric matrix. With sufficiently thin dielectric layers between FM granules or if the matrix material separating the magnetic granules from each other is a nonmagnetic conductor, the system has electrical conductivity. In the first case, the percolation current arises with a decrease in temperature as the thermally activated tunneling in transport channels becomes difficult. In the second case, percolation arises when the magnetic field decreases, and the magnetic moments of particles become disoriented, leading to a decrease in probability of electron transition between neighboring ferromagnetic granules. Figure 18 schematically shows magnetic granules placed in an insulating matrix in zero field (a) and the saturation field (b). The magnetic moments of the granules distributed randomly in zero field are aligned in one direction when an external field is applied, and when

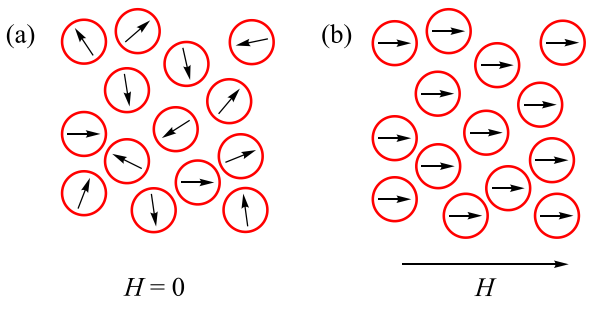

Fig. 18. Schematic representation of magnetic granules in zero field (a) and in saturation field (b).

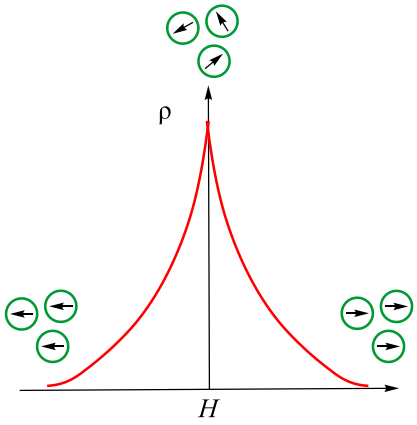

Fig. 19. Schematic dependence of the resistance of a granular system on the magnetic field.

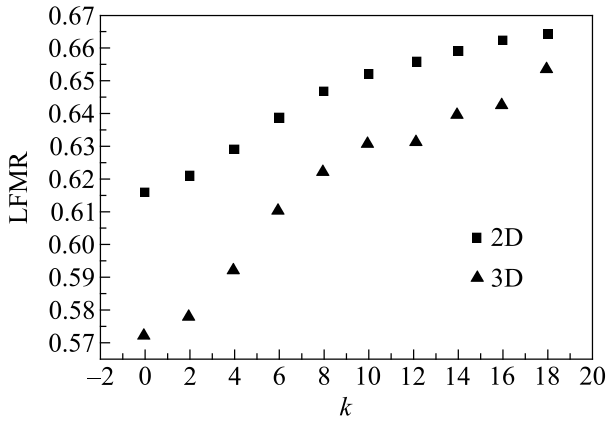

Fig. 20. Dependences of LFMR on the disorder parameter k for two-dimensional (30^2 particles) and three-dimensional (10^3 particles) systems [70].

the magnetic field is removed, they again become misoriented due to thermal fluctuations. Figure 19 schematically shows the magnetic field dependence of the resistance for a granular magnetic/insulator system. The maximum resistance of such a system corresponds to a zero field, in which the magnetic moments of the granules are oriented randomly. The gradual alignment of magnetic moments along the field increases the probability of electron tunneling between the granules and thereby decreases the resistance of the system. In this case, the resistance decreases, i.e., there is an increase in negative MR (Fig. 19). However, the ideal picture shown in Fig. 19 does not coincide with what is observed in the experiment. The real maximum resistance in powder samples is indeed observed in zero field, but only once, in the initial, completely demagnetized state of the sample. Subsequently, hysteresis curves of magnetoresistance are observed, in which there are two maxima corresponding to the coercive fields during magnetization reversal of the sample. In this case, the maximum increase in resistance when the magnetic field is applied is observed in the region of low fields (see Fig. 17).

In Ref. 70, the Monte Carlo method for an arbitrary grid of resistors (Miller–Abrahams network) simulated magnetotransport properties in 2D and 3D granular ferromagnets. In these calculations, it was assumed that the conductivity between pairs of neighboring granules depends both on the intergranular distance kr_{ij} [assuming that $\sigma \propto \exp(-kr_{ij})$, where k is the measure of spatial disorder, and r is a random number with uniform distribution in the range (0,1)] and the relative orientation θ_{ij} of the magnetization vectors in neighboring granules [assuming $\sigma \propto (1+\cos\theta_{ij})^2$]. The sensitivity of the system to removing an arbitrary single contact may be characterized by the resistance ratio R_{cut}/R, where R is the initial resistance of the Miller–Abrahams network, and R_{cut} is the same resistance of network after removal of an arbitrary resistor from the system. A comparison of the results obtained with the behavior of a real sample — a Ni film consisting of $\sim 10^{10}$ metal granules — showed that, in the regime of strong disorder, the total conductivity of the system could be controlled by a single dominating path through which the main current flows.

The authors also showed that in semilogarithmic coordinates, the average value of the relative change in the resistances of a random resistor network obeys the scaling relation $\ln(\overline{R_{cut}/R}) = f(k^n/L)$, where L is the dimension of the system and ν ($\nu = 4/3$ for 2D case and ≈ 0.88 for 3D case) is the critical exponent of the percolation correlation length $\xi \propto (p - p_c)^{-\nu}$ [71].

The magnitude of low-field MR (LFMR) increased with an increase in the degree of disorder k. The higher k values correspond to more disordered (diluted) samples. The effect of magnetoresistance strengthening at the percolation threshold was attributed by the authors of [70] to the instantaneous switching of the current paths in the sample due to the influence of magnetic field on the "critical grain" connecting the parts of the percolation cluster.

Similar results were obtained in [72] when solving the system of Kirchhoff equations for 2D and 3D random rectangular resistor grids for numerical simulation of the current distribution of LFMR in granular ferromagnetic semimetals. The author has shown that an increase in the degree of disorder leads to an increase in the current localization. This process is accompanied by an increase in LFMR. Moreover, there is a close connection between the LFMR value and the current morphology. In the limit of strong disorder, a quasi-one-dimensional transport channel is formed, and the LFMR reaches its maximum. Figure 20 shows the dependence of the LFMR value for half-metals on the degree of disorder k. It can be seen that LFMR increases with k and reaches saturation at $k \approx 18$. An increase in disorder leads to current localization both in zero field [Fig. 21 [72]] and in a finite external field $H = H_{ext}$ [Fig. 22 [72]]. In Figs. 21 and 22, the intensity of the bond color indicates the magnitude of the current. The black lines correspond to the maximum current, green lines correspond to the minimum.

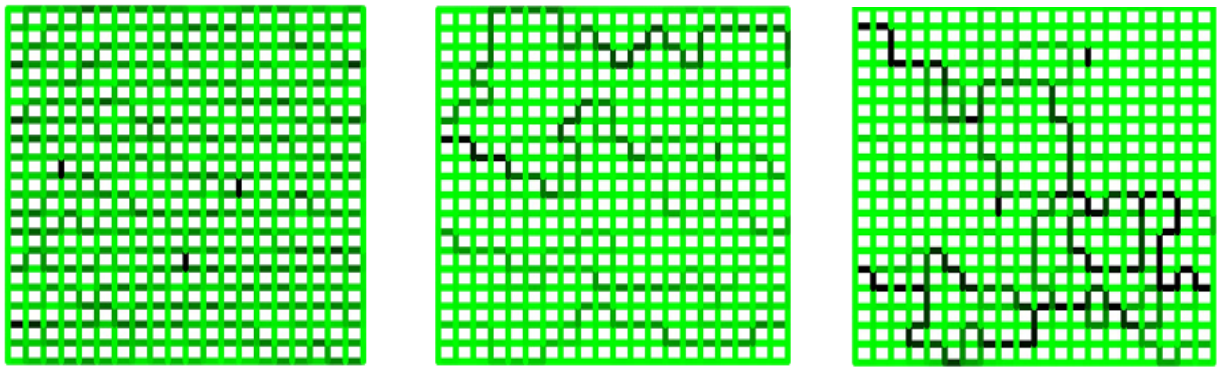

$k = 0.001$ (a) $k = 5$ (b) $k = 15$ (c)

Fig. 21. Current morphology in a system without an external magnetic field ($H = 0$) for different values of the disorder parameter k [72].

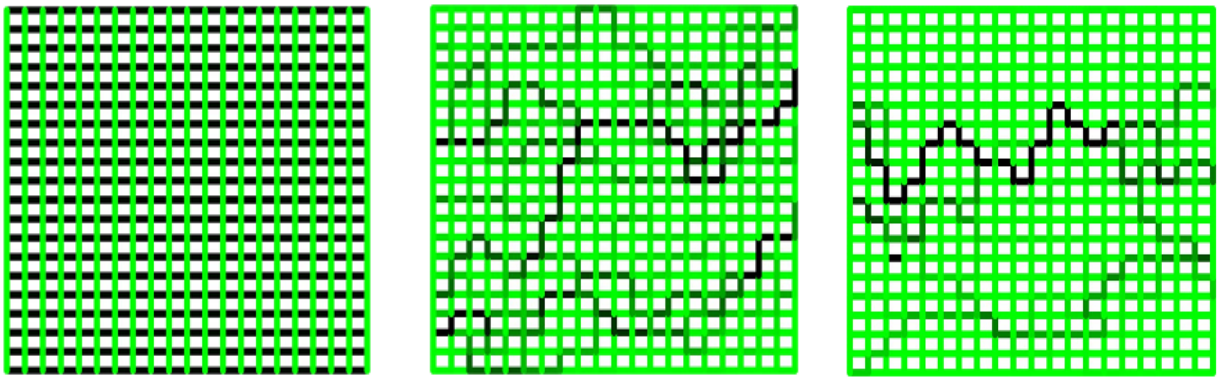

$k = 0$ (a) $k = 5$ (b) $k = 15$ (c)

Fig. 22. Current morphology in a system with external magnetic field $H = H_{ext}$ for different values of the disorder parameter k [72].

The electrical conductivity of composite systems, which are a complex combination of the conducting and dielectric phases, is determined by two mechanisms: percolation in continuous channels of the conducting phase [73] and/or tunneling between insulated conductive layers (grains) [58, 74, 75]. In real granular systems, these two mechanisms work together. Wherein, tunneling blurs the classical percolation threshold, determined according to the Miller–Abrahams model as the concentration of broken bonds, at which an infinite percolation cluster, that provides metallic conductivity in the system, disappears [76]. Since the theories proposed to explain the electrical conductivity beyond the percolation threshold took into account tunneling only between one pair of neighboring particles, the relationship between the magnitudes of the magnetoresistance and electrical conductivity for the network of tunneling contacts has not been discussed. The TMR value in the models considered in Refs. 58, 74, 75 did not depend on the system impedance. However, this result does not agree with the observation of the increase in LFMR near the percolation threshold.

The authors of the paper [72], based on their calculations of the dependence of LFMR and current morphology on the degree of disorder, come to the conclusion that the appearance of the LFMR maximum near the percolation threshold in half-metal composites [64, 74, 75] is a consequence of the current localization in the sample and is directly related to the transport in a quasi-one-dimensional conducting channel.

Thus, the simulation of magnetotransport properties of disordered half-metals by a random grid of resistors provides an argument in favor of the percolation mechanism of LFMR in these systems. Currently, the main hypothesis is that the rise of LFMR in composite systems based on half-metals may be related to the current localization in the sample, and the maximum of LFMR near the percolation threshold is a consequence of charge carriers transfer along a quasi-one-dimensional path.

In Ref. 77, MR was studied in samples of granular ferromagnets containing a small number of grains (about 100). The experiments carried out on cold-deposited Ni island films of mesoscopic size (less than 0.5×0.5 μm) showed

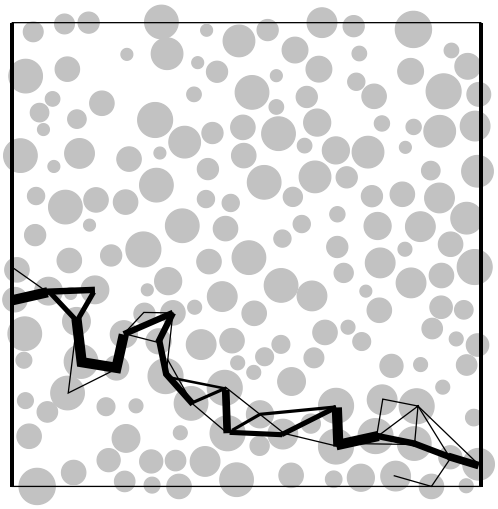

Fig. 23. The simulation of current trajectories in a mesoscopic sample containing 180 grains shows a single dominant trajectory [77]. A small dc voltage is applied to two wires connected to the sample on the left and right sides. The line width is proportional to the amount of current passing through the sample.

that, in comparison to macroscopic ones, mesoscopic granular samples exhibited unusually strong saturation fields and a wide spread of MR values, in some cases exceeding the MR of macroscopic samples up to 7 times. The authors show that for mesoscopic samples, the evolution of the MR curves with a decrease in the distance between grains is qualitatively different from the MR evolution for large samples. Analyzing the results, the authors suggested that this behavior reflects the transition from percolation conductivity to conductivity with a predominating quasi-single-channel transport (Fig. 23). It is generally acknowledged that a decrease in the size of any disordered system so much, that it come into a mesoscopic regime is always accompanied by a large number of unusual "mesoscopic" phenomena.

A similar change in the current path routes with a decrease in the applied voltage, which leads to the behavior pertinent to a one-dimensional conducting chain and subsequent transition to the strong localization mode, has also been observed on two-dimensional percolation gold films in [78, 79].

The rise in low-field magnetoresistance with decreasing temperature is not a feature of CrO_2 or half-metals only. Presumably, this is a common property of granular magnetic systems. For example, an increase in the low-field magnetoresistance value with decreasing temperature is observed in granular samples of the magnetic superconductor $RuSr_2(Gd_{1.5}Ce_{0.5})Cu_2O_{10-\delta}$ [80, 81]. It is also possible that the system does not necessarily have to be granular. For the increase in magnetoresistance with decreasing temperature, the mere by presence of hopping conductivity may be enough. The magnetic and resistive measurements carried out on the single-crystal samples of $La_{2-x}Sr_xCuO_4$ showed that with a decrease in the concentration of strontium impurity, the degree of "extrinsically induced" disorder and the degree of structural disorder increase. As a result, the nonlinear behavior of the conductivity and an increase in the magnetoresistance intensified both with decreasing strontium content and with decreasing temperature [82].

The change in the shape of the magnetoresistance hysteresis loops with decreasing temperature, which was found in work [83], presumably, also belongs to the phenomena associated with current channels switching (Fig. 24). As remarked in [84], the reason for the temperature evolution of hysteresis loops in samples with percolation conductivity is that the sequence of formation and decay of current-carrying channels during the magnetic field increasing and decreasing may not coincide. That leads to the appearance of an additional magnetoresistive hysteresis in the domain of magnetic fields higher than H_p (where H_p corresponds to the fields of magnetoresistance maxima) due to the switching of a small number of percolation current channels at sufficiently low temperatures and also due to the appearance of an additional overlap of the magnetoresistance curves with decreasing temperature. At low temperatures, the sequence of the appearance and disappearance of percolation current

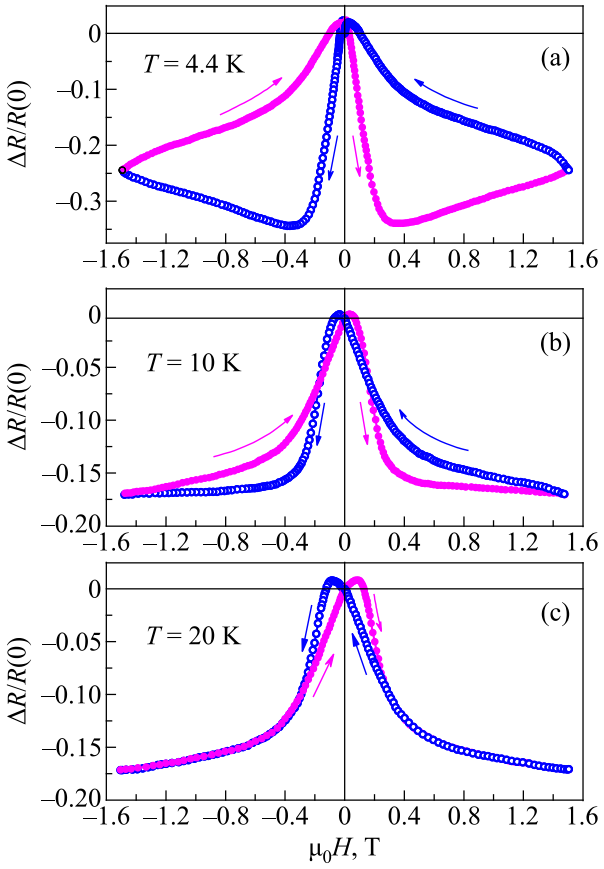

Fig. 24. Hysteresis curves of the MR of a composite of pressed CrO_2 nanoparticles coated with Cr_2O_3 shells 1.6 nm thick at: $T = 4.4$ (a), 10.0 (b), 20.0 (c) K. Arrows indicate the direction of change in the magnetic field when recording MR curves [66].

channels in the magnetic fields above H_p is different when the magnetic field is introduced into and removed from the system. Under these conditions, a large area of magnetoresistive hysteresis loops is observed. With increasing temperature, the number of current paths through the sample increases and, consequently, the current distribution within the sample becomes more uniform. In this case, additional points of intersection of the magnetoresistive hysteresis loops disappear, and the area of the hysteresis loop decreases (Fig. 24). Furthermore, at low temperatures, the application of an external magnetic field by itself can also open additional transport channels [72], which is likewise the reason for the giant low-field magnetoresistance in such percolation systems.

The authors of the paper [63] carried out an exciting experiment, diluting a nanopowder of needle-like particles of a half-metal CrO_2 by nanoparticles of antiferromagnetic insulator Cr_2O_3 with the same particle size and shape. They fitted the results to the dependence $\rho \propto (x - x_p)^2$ known in the percolation theory [85] and showed that the threshold concentration for CrO_2 nanoparticles is $x_p \approx 0.23$. The authors found that dilution of CrO_2 with dielectric particles leads to an increase in both resistance and TMR values (Fig. 17). The sample with a CrO_2 concentration $x \approx 0.25$, located near the percolation threshold, but still on the metallic side, had a resistivity value by three orders of magnitude higher than pure CrO_2 and its TMR, at $T = 0$ and $H \to \infty$, could be extrapolated to a value of 56%. As evidence, the authors demonstrate the temperature dependence of the relative TMR in the inset to Fig. 17, which shows the temperature dependence of TMR in pressed nanopowder $(CrO_2)_{0.25} + (Cr_2O_3)_{0.75}$ [59].

Another consequence of the percolation behavior is that in the low-temperature domain, the field of maximum for magnetoresistance behavior in powder samples may not coincide with the coercive force measured by a magnetometer (Fig. 25). The reason for this discrepancy lies in the low-temperature peculiarities of percolation conductivity. When the temperature decreases, the current path with the least number of tunnel gaps becomes dominant. So, the percolation cluster tends to include longest (largest) particles, which are usually multidomain by its nature. As a result, with decreasing temperature, the percolation cluster congregates multidomain particles, in which the process of magnetization reversal is facilitated due to the mechanism of domain walls motion. Thus, when the temperature drops, some selection takes place among all the granules. In this case, the "ensemble-averaged" coercive field for the longest needle-shaped particles included in the percolation cluster is less than the coercive field measured by a magnetometer, which is "averaged over the whole specimen" [86, 87].

The low-temperature discrepancy between the coercive fields for the whole specimen and the magnetic fields, corresponding to its magnetoresistance maxima, found in Refs. 86, 87, has not been observed in [63], where the magnetoresistance of CrO_2–Cr_2O_3 powder mixtures was studied. A possible reason is that $(CrO_2)_{0.25} + (Cr_2O_3)_{0.75}$ powder mixture studied in [63] was initially on the metal side of the metal–insulator transition, and the percolation cluster formed by chromium dioxide particles does not lose connectivity even at the lowest temperatures. On the contrary, in [86, 87], not a mechanical mixture of nanoparticles was studied, but a pressed composite in which CrO_2 particles were encapsulated in Cr_2O_3 dielectric shells. Thus, an infinite percolation cluster did not exist in this material from the very beginning, and charge transport was carried out exclusively by spin-dependent electron tunneling through thin dielectric shells covering the CrO_2 particles.

The complete scenario of percolation magnetotransport in disordered half-metals must undoubtedly include

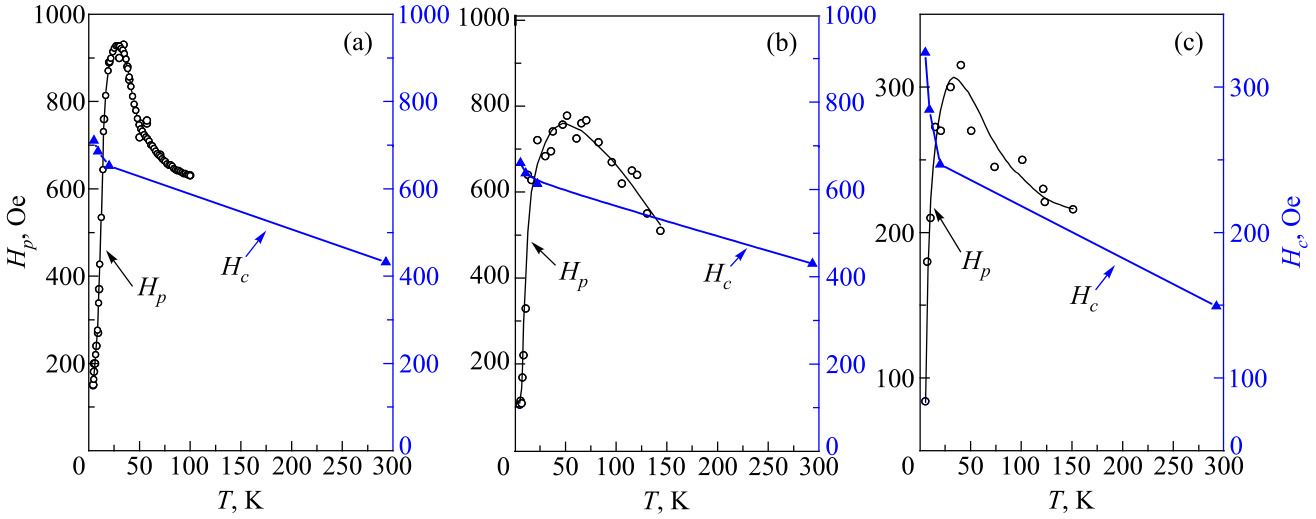

Fig. 25. The ratio $H_p \approx H_c$ expected and observed for compressed powders with small (submicron) particle sizes is not fulfilled at low temperatures ($T < 50$ K) for needle-shaped CrO_2 particles covered with 1.73 nm (a) and 1.58 nm (b) β-CrOOH dielectric shell, and round-shaped CrO_2 particles covered with 3.6 nm β-CrOOH dielectric shell (c). There is a sharp decrease in H_p with lowering the temperature (○) compared with coercive force H_c (▲) taken from magnetic measurements [86].

the effects of Coulomb blockade, which intensify with decreasing temperature. In particular, the authors of [65] believed that the temperature dependence of the resistance $\rho \propto \exp(\Delta'/T)^{1/2}$ for $T < 35$ K is typical of the mechanism of intergranular tunneling due to the Coulomb gap $\Delta' = 5$ K, which gives a dominant contribution at low temperatures. However, for $T > 35$ K, a new "spin-independent" channel opens, associated with the inelastic mechanism of hopping conduction over localized states inside the barrier. The authors of [63] came to similar conclusions. According to their evaluation, the charging energy for the granules $\Delta' = 13$ K. They substantiated the conclusions on the Coulomb gap influence by the similarity of the temperature and electric field dependences of resistance. They also showed that the Coulomb gap value depends on the magnetic field and increases with disordering of the magnetic moments of CrO_2 particles in their powder sample. In this way, they confirmed the conclusions of Ref. 58, in which the magnetic contribution to the Coulomb energy had been interpreted as a change in the exchange interaction energy for two neighboring magnetically disordered particles containing n and n' electrons, as a result of a transfer of one electron between them.

9. Anisotropic magnetoresistance in compacted powder composites

As it was noted at the end of Sec. 4, magnetocrystalline anisotropy with easy magnetization axis c is inherent for CrO_2 epitaxial films and crystallites. There is a widespread opinion that in powder materials consisting of many well-mixed and randomly oriented particles, the anisotropy should disappear in the theoretical limit. However, the experiment described in [54] witnessed that magnetoresistance in compacted powders is substantially anisotropic.

As shown in [54], the main reason for the observed anisotropy of transport properties in compacted powder composites (see Fig. 26) is the anisotropy of the shape of the particles of which they are composed. The chromium dioxide crystallites are characterized by an acicular shape, elongated along the c axis, which is at the same time an easy magnetization axis. Due to uniaxial compression during the powder compaction, the needle-shaped particles tend to be oriented perpendicular to the applied load [54, 88]. Accordingly, the pressing axis becomes the hard magnetization axis for the obtained powder sample. Thus, the observed anisotropy turns out to be directly related to the value of the magnetic susceptibility in the chosen direction relative to the applied magnetic field (see Fig. 27). We should add that the uniaxial compression affects the tunneling transport properties not only through the shape anisotropy but even directly. For example, Fig. 27(a) shows that a small value of anisotropy at the 6% level is still observed even for the sample with spherical particles. In this experiment, the chromium dioxide particles were modified at the stage of nucleation, so that they crystallized in a spherical form. The resulting rounded CrO_2 particles coated with a 3.6 nm thick Cr_2O_3 dielectric layer were 120 nm in diameter. Still, despite the spherical shape of CrO_2 particles, the pressed samples exhibited small anisotropy, apparently related to the density tensor anisotropy, which arose from uniaxial compression.

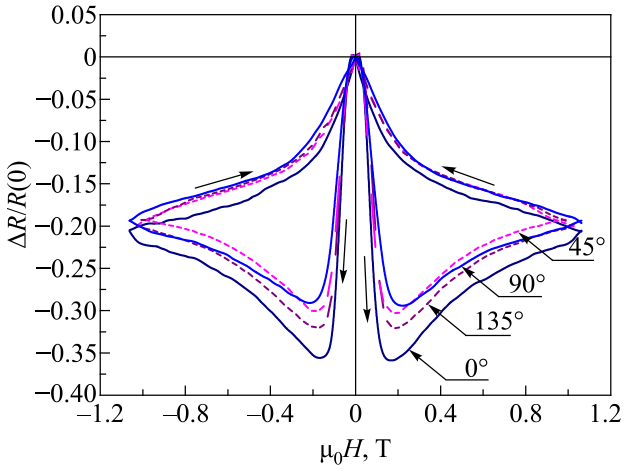

Fig. 26. TMR hysteresis loops for compacted powder sample at different orientations of the magnetic field relative to the sample plane [54].

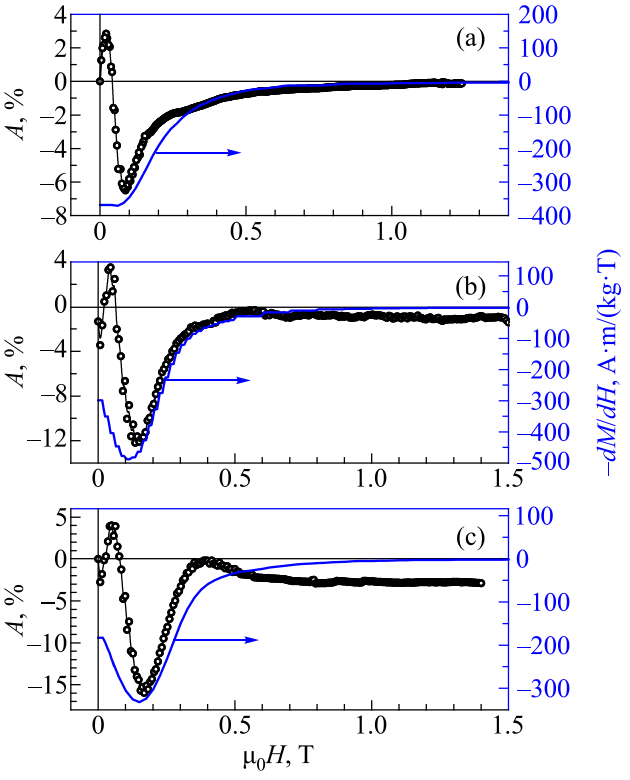

Fig. 27. The dependences of the anisotropy $A = [R(H_{\parallel}) - R(H_{\perp})]/R(0)$ and the magnetic susceptibility dM/dH on the magnetic field at $T = 4.2$ K for three different compacted powder samples: ~120 nm CrO_2 spherical particles in 3.6 nm β-CrOOH dielectric shell (a), ~ 302×24 nm CrO_2 prismatic particles in 0.8 nm (b) and 1.2 nm (c) β-CrOOH dielectric shell [54].

Conclusion

More than 30 years have passed since discovering the giant magnetoresistance effect in multilayer systems with ferromagnetic contacts [2, 3]. During this time, significant progress was achieved in understanding the nature of this phenomenon. Almost simultaneously with the experimental discovery of the GMR effect, the corresponding theoretical concepts were developed in Refs. 11 and 18.

Prospects for practical use aroused after Miyazaki [12] and Moodera [13] showed in 1994 that the magnitude of the GMR effect can be significantly increased (up to 30%) due to the quantum tunneling effect if a dielectric layer is used instead of a nonmagnetic metal separating two ferromagnets.

The largest values of the magnetoresistive effect were obtained using ferromagnets with a high degree of spin polarization. The maximum magnitude of the effect (up to 600% at room temperature) [14–16] appears in epitaxially grown magnetic tunnel structures based on MgO dielectric barrier. The practical use of magnetic tunnel junctions in the reading elements of magnetic disk memory led to a significant increase in storage areal density of magnetic media.

In parallel with the study of single magnetic tunnel contacts, the properties of powder composites were studied [63]. From the point of view of an experimental physicist, despite the complexity of the theoretical description of their electron-transport properties, the advantage of such materials is their availability for research and a wide range of experimental parameters (sizes of nanoparticles, thickness and material of their dielectric coatings, proximity to the percolation threshold for mixtures of conducting and nonconducting phases) that may be changed. The created composites are of considerable interest for studying the peculiarities of charge transport in percolation magnetic tunnel structures with the prospect of using the obtained results in powerful spintronic devices to regulate spin-polarized current and creating materials for random access memory (MRAM) based on magnetoresistive effects.

In terms of technology development, pressed powder composites, combined with modern powder metallurgy methods, are promising for creating high-tech functional materials with predefined properties.

Thus, the results considered in the review are of both fundamental and practical interest. The high values of tunneling magnetoresistance (up to 40% [54]) experimentally found in some samples of pressed nanoparticles allow us to hope for the successful use of CrO_2 powder nanocomposites in spintronic devices. Besides, the anisotropy of the coercive force relative to the pressing axis of the samples reveals the possibilities of using nanostructured surfaces consisting of needle-like nanoparticles as a basis for creating magnetic data carriers with increased storage areal density. Further increase in the density can be achieved by introducing a small amount of iron into chromium dioxide crystal lattice in order to increase the coercive force [89].

Simultaneously, on the way to the practical use of CrO_2 powder nanocomposites, there are several poorly studied and not fully understood problems. Among them it should be mentioned:

(i) The effect of low-field magnetoresistance [72, 77];

(ii) The influence of crystal structure distortions and impurities near the interface on the tunneling properties of magnetic contacts [12, 66];

(iii) The understudied variety of hysteresis phenomena at low temperatures [66, 85], when a sharp initial increase in negative magnetoresistance in low fields is replaced by its subsequent fall, starting from a relatively low field $H_{max} \cong 0.2$ T (this effect is especially noticeable at low temperatures and low measurement currents);

(iv) The change in the ratio between the fields of magnetoresistance maxima and the magnitude of coercive field with temperature variation [87].

All these features in the behavior of chromium dioxide powder nanocomposites require further studying.

Acknowledgments

The work was supported by the project No. 2/20-H «Development and Research of Promising Nanostructured Objects for Quantum Engineering» within the framework of the target program of fundamental research of the National Academy of Sciences of Ukraine «Prospective Basic Research and Innovative Development of Nanomaterials and Nanotechnologies for the Needs of Industry, Healthcare, and Agriculture» for 2021.

1. I. I. Mazin, *Phys. Rev. Lett.* **83**, 1427 (1999).
2. M. N. Baibich, J. M. Broto, A. Fert, F. Nguyen Van Dau, F. Petroff, P. Etienne, G. Creuzet, A. Friederich, and J. Chazelas, *Phys. Rev. Lett.* **61**, 2472 (1988).
3. G. Binasch, P. Grünberg, F. Saurenbach, and W. Zinn, *Phys. Rev. B* **39**, 4828(R) (1989).
4. R. E. Camley and J. Barnaś, *Phys. Rev. Lett.* **63**, 664 (1989).
5. V. Ya. Kravchenko, *JETP* **121**, 703 (2002) (in Russian).
6. P. M. Levy, S. Zhang, and A. Fert, *Phys. Rev. Lett.* **65**, 1643 (1990).
7. A. Vedyayev, B. Dieny, and N. Ryzhanova, *Europhys. Lett.* **19**, 329 (1992).
8. Yu. A. Shkurdoda, L. V. Dekhtyaruk, and V. B. Loboda, *Functional Materials* **15**, 38 (2008).
9. L. V. Dekhtyaruk, *Metallofiz. Latest Technol.* **30**, 219 (2008) (in Russian).
10. S. S. Aplesnin, *Fundamentals of Spintronics: Textbook*, 2nd ed., SPb., Publishing house “Lan” (2010) (in Russian).
11. M. Julliere, *Phys. Lett. A* **54**, 225 (1975).
12. T. Miyazaki and N. Tezuka, *J. Magn. Magn. Mater.* **139**, L231 (1995).

13. J. S. Moodera, L. R. Kinder, T. M. Wong, and R. Meservey, *Phys. Rev. Lett.* **74**, 3273 (1995).
14. S. G. Wang, R. C. C. Ward, T. Hesjedal, X.-G. Zhang, C. Wang, A. Kohn, Q. L. Ma, J. Zhang, H. F. Liu, and X. F. Han, *J. Nanosci. Nanotechnol.* **12**, 1006 (2012).
15. S. S. P. Parkin, C. Kaiser, A. Panchula, P. M. Rice, B. Huges, M. Samant, and S.-H. Yang, *Nature Mater.* **3**, 862 (2004).
16. S. Ikeda, J. Hayakawa, Y. Ashizawa, Y. M. Lee, K. Miura, H. Hasegawa, M. Tsunoda, F. Matsukura, and H. Ohno, *Appl. Phys. Lett.* **93**, 082508 (2008).
17. J. Bardeen, *Phys. Rev. Lett.* **6**, 57 (1961).
18. J. C. Slonczewski, *Phys. Rev. B* **39**, 6995 (1989).
19. R. Meservey and P. M. Tedrow, *Phys. Rep.* **238**, 173 (1994).
20. J. M. D. Coey and M. Venkatesan, *J. Appl. Phys.* **91**, 8345 (2002).
21. S. P. Lewis, P. B. Allen, and T. Sasaki, *Phys. Rev. B* **55**, 10253 (1997).
22. R. A. de Groot, F. M. Mueller, P. G. van Engen, and K. H. J. Buschow, *Phys. Rev. Lett.* **50**, 2024 (1983).
23. T. Saitoh, M. Nakatake, A. Kakizaki, H. Nakajima, O. Morimoto, Sh. Xu, Y. Moritomo, N. Hamada, and Y. Aiura, *Phys. Rev. B* **66**, 035112 (2002).
24. R. Weht and W. E. Pickett, *Phys. Rev. B* **60**, 13006 (1999).
25. M. Penicaud, B. Silberchiot, C. B. Sommers, and J. Kubler, *J. Magn. Magn. Matter* **103**, 212 (1992).
26. B. Nadgorny, I. I. Mazin, M. Osofsky, R. J. Soulen, P. Broussard, R. M. Stroud, D. J. Singh, V. G. Harris, A. Arsenov, and Ya. Mukovskii, *Phys. Rev. B* **63**, 4433 (2001).
27. D. J. Singh, *Phys. Rev. B* **55**, 313 (1997).
28. J. Kuneš, *J. Phys.: Condens. Matter* **27**, 333201 (2015).
29. R. J. Soulen, J. M. Byers, M. C. Osofsky, B. Nadgorny, T. Ambrose, S. F. Cheng, P. R. Broussard, C. T. Tanaka, J. Nowak, J. S. Moodera, A. Barry, and J. M. D. Coey, *Science* **282**, 85 (1998).
30. H. Öztürk and C. Kürkçü, *Acta Physica Polonica A* **136**, 26 (2019).
31. J. K. Burdett, G. J. Miller, J. W. Richardson, and J. V. Smith, *J. Am. Chem. Soc.* **110**, 8064 (1988).
32. M. A. Korotin, V. I. Anisimov, D. I. Khomskii, and G. A. Sawatzky, *Phys. Rev. Lett.* **80**, 4305 (1998).
33. K. Schwarz, *J. Phys. F: Metal Physics* **16**, L211 (1986).
34. Yu. A. Uspenskii, E. T. Kulatov, and S. V. Halilov, *Phys. Rev. B* **54**, 474 (1996).
35. B. L. Chamberland, *Journal Critical Reviews in Solid State and Materials Sciences* **7**, 1 (1977).
36. A. Barry, *CrO_2: A General Study*, Ph. D. Thesis (1999).
37. A. Barry and J. M. D. Coey, *J. Appl. Phys.* **83**, 7166 (1998).
38. P. Lubitz, M. Rubinstein, M. S. Osofsky, B. E. Nadgorny, R. J. Soulen, and K. M. Bussmann, *J. Appl. Phys.* **89**, 6695 (2001).
39. F. Y. Yang, C. L. Chien, and E. F. Ferrari, *Appl. Phys. Lett.* **77**, 286 (2000).
40. D. S. Rodbell, J. M. Lommel, and R. C. DeVries, *J. Phys. Soc. Jpn.* **21**, 2430 (1966).
41. S. M. Watts, S. Wirth, S. von Molnár, A. Barry, and J. M. D. Coey, *Phys. Rev. B* **61**, 9621 (2000).
42. A. Gupta, *J. Appl. Phys.* **87**, 6073 (2000).
43. P. A. Stampe and R. J. Kennedy, *J. Appl. Phys.* **89**, 7696 (2001).
44. T. Kasuya, *Progr. Theor. Phys.* **22**, 227 (1959).
45. K. Kubo and N. Ohata, *J. Phys. Soc. Jpn.* **33**, 21 (1972).
46. X. Wang and X.-G. Zhang, *Phys. Rev. Lett.* **82**, 4276 (1999).
47. X. W. Li, A. Gupta, T. R. McGuire, and P. R. Duncombe, *J. Appl. Phys.* **85**, 5585 (1999).
48. I. I. Mazin, D. J. Singh, and C. Ambrosch-Draxl, *Phys. Rev. B* **59**, 411 (1999).
49. U. Rüdiger, M. Rabe, K. Samm, B. Özyilmaz, J. Pommer, M. Fraune, and G. Güntherodt, *J. Appl. Phys.* **89**, 7699 (2001).
50. K. Suzuki and P. M. Tedrow, *Phys. Rev. B* **58**, 11597 (1998).
51. K. Suzuki and P. M. Tedrow, *Appl. Phys. Lett.* **74**, 428 (1999).
52. M. A. Korotin, V. I. Anisimov, D. I. Khomskii, and G. A. Sawatzky, *Phys. Rev. Lett.* **80**, 4305 (1998).
53. A. Urushibara, Y. Moritomo, T. Arima, A. Asamitsu, G. Kido, and Y. Tokura, *Phys. Rev. B* **51**, 14103 (1995).
54. N. V. Dalakova, E. Yu. Belyaev, O. M. Bludov, V. A. Gorelyi, O. M. Osmolovskaya, and M. G. Osmolovskiy, *Fiz. Nizk. Temp.* **44**, 1510 (2018) [*Low Temp. Phys.* **44**, 1180 (2018)].
55. N. V. Dalakova, A. N. Bludov, E. Yu. Beliayev, V. A. Horielyi, O. M. Osmolowskaya, and M. G. Osmolowsky, *Bull. Russ. Acad. Sci. Phys.* **81**, 278 (2017).
56. C. König, M. Fonin, M. Laufenberg, A. Biehler, W. Bührer, M. Kläui, U. Rüdiger, and G. Güntherodt, *Phys. Rev. B* **75**, 144428 (2007).
57. N. V. Volkov, *Phys.-Usp.* **182**, 263 (2012).
58. J. S. Helman and B. Abeles, *Phys. Rev. Lett.* **37**, 1429 (1976).
59. J. M. D. Coey, *J. Appl. Phys.* **85**, 5576 (1999).
60. A. Barry, J. M. D. Coey, and M. Viret, *J. Phys.: Condens. Matter* **12**, L173 (2000).
61. A. Gupta, X. W. Li, and G. Xiao, *Appl. Phys. Lett.* **78**, 1894 (2001).
62. H. Y. Hwang and S.-W. Cheong, *Science* **278**, 1607 (1997).
63. J. M. D. Coey, A. E. Berkowitz, Ll. Balcells, F. F. Putris, and A. Barry, *Phys. Rev. Lett.* **80**, 3815 (1998).
64. S. Manoharan, D. Elefant, G. Reiss, and J. B. Goodenough, *Appl. Phys. Lett.* **72**, 984 (1998).
65. J. Dai and J. Tang, *Phys. Rev. B* **63**, 054434 (2001).
66. N. V. Dalakova, B. I. Belevtsev, E. Yu. Beliayev, A. N. Bludov, V. N. Pashchenko, M. G. Osmolovsky, and O.M. Osmolovskaya, *Fiz. Nizk. Temp.* **38**, 1422 (2012) [*Low Temp. Phys.* **38**, 1121 (2012)].
67. W. J. DeSisto, P. R. Broussard, T. F. Ambrose, B. E. Nadgorny, and M. S. Osofsky, *Appl. Phys. Lett.* **76**, 3789 (2000).
68. Y. Ji, G. J. Strijkers, F. Y. Yang, C. L. Chien, J. M. Byers, A. Anguelouch, Gang Xiao, and A. Gupta, *Phys. Rev. Lett.* **86**, 5585 (2001).
69. M. Hammersley and D. J. A. Welsh, *First-Passage Percolation, Subadditive Processes, Stochastic Networks, and Generalized Renewal Theory*, In: Bernoulli–Bayes–Laplace Anniversary Volume, J. Neyman and L. M. Le Cam (eds.), Springer-Verlag, Heidelberg (1965), p. 61.
70. Y. M. Strelniker, S. Havlin, R. Berkovits, and A. Frydman, *J. Appl. Phys.* **99**, 08P905 (2006)

71. B. I. Shklovskii and A. L. Efros, *Electronic Properties of Doped Semiconductors*, Springer, New York (1984); D. Stauffer and A. Aharony, *Introduction to Percolation Theory*, Taylor and Francis, London (1992); *Fractals and Disordered Systems*, 2nd ed., A. Bunde and S. Havlin (eds.) Springer, Heidelberg (1996).
72. Sheng Ju, Tian-Yi Cai, and Z. Y. Li, *Appl. Phys. Lett.* **87**, 172504 (2005).
73. J. Inoue and S. Maekawa, *Phys. Rev. B* **53**, R11927 (1996).
74. M. Ziese, *Rep. Prog. Phys.* **65**, 143 (2002).
75. M. Venkatesan, P. Velasco, J. A. Alonso, J. L. Martínez, and J. M. D. Coey, *J. Phys.: Condens. Matter* **16**, 3465 (2004).
76. *Synthesis, Structure and Properties of Metal / Semiconductor Containing Nanostructured Composites*, L. I. Trakhtenberg and M. Ya. Melnikov (eds.), Technosphere, Moscow (2016).
77. A. Y. Dokow, H. Vilchik, and A. Frydman, *Phys. Rev. B* **72**, 094402 (2005).
78. B. I. Belevtsev, E. Yu. Belyaev, Yu. F. Komnik, and E. Yu. Kopeichenko, *Fiz. Nizk. Temp.* **23**, 965 (1997) [*Low Temp. Phys.* **23**, 724 (1997)].
79. B. I. Belevtsev, E. Yu. Beliayev, and Yu. A. Kolesnichenko, *Int. J. Mod. Phys. B* **27**, 1350026 (2013).
80. B. I. Belevtsev, E. Yu. Beliayev, D. G. Naugle, K. D. D. Rathnayaka, M. P. Anatska, and I. Felner, *J. Phys.: Condens. Matter* **19**, 036222 (2007).
81. V. B. Krasovitsky, B. I. Belevtsev, E. Yu. Beliayev, D. G. Naugle, K. D. D. Rathnayaka, and I. Felner, *J. Phys.: Conf. Series* **51**, 283 (2006).
82. N. V. Dalakova, B. I. Belevtsev, E. Yu. Belyaev, and A. S. Panfilov, *Fiz. Nizk. Temp.* **40**, 513 (2014) [*Low Temp. Phys.* **40**, 397 (2014)].
83. B. I. Belevtsev, N. V. Dalakova, M. G. Osmolowsky, E. Yu. Beliayev, and A. A. Selutin, *Bull. Russ. Acad. Sci. Phys.* **74**, 1062 (2010).
84. B. I. Belevtsev N. V. Dalakova, M. G. Osmolowsky, E. Yu. Beliayev, and A. A. Selutin, *J. Alloys Compd.* **479**, 11 (2009).
85. K. Stauffer, *Introduction to Percolation Theory*, Taylor and Francis, London (1985).
86. N. V. Dalakova, E. Yu. Beliayev, and V. A. Horielyi, *East Eur. J. Phys.* **4**, 78 (2017).
87. N. V. Dalakova, E. Yu. Beliayev, V. A. Horielyi, O. M. Osmolovskaya, and M. G. Osmolowsky, *Bull. Russ. Acad. Sci. Phys.* **83**, 778 (2019).
88. N. V. Dalakova, E. Y. Beliayev, O. M. Osmolovskaya, M. G. Osmolowsky, and V. A. Gorelyy, *Bull. Russ. Acad. Sci. Phys.* **79**, 789 (2015).
89. N. V. Dalakova, E. Yu. Beliayev, Yu. A. Kolesnichenko, V. A. Horielyi, O. M. Osmolovskaya, and M. G. Osmolowsky, *Bull. Russ. Acad. Sci. Phys.* **80**, 664 (2016).

Магнітотранспортні властивості порошкових композиційних матеріалів на основі двоокису хрому
(Огляд)

E. Yu. Beliayev, V. A. Horielyi, Yu. A. Kolesnichenko

Представлено найбільш значущі експериментальні результати та теоретичні концепції, що стосуються композитів на основі діоксиду хрому, відповідно до їх впливу на еволюцію сучасного розуміння явищ транспорту електронів у невпорядкованих магнітних системах. Показано, що різноманітність фізичних процесів, що відбуваються в порошкових матеріалах, не дозволяє виробити цілісний теоретичний підхід до опису властивостей отриманих ущільнених матеріалів. Властивості композиційних матеріалів залежать від анізотропії форми та магнітних властивостей частинок, з яких вони складаються. Вплив ефектів перколяції призводить до зміни морфології струмопровідних каналів із зміною температури в зовнішньому магнітному полі. Це впливає як на форму петель гістерезису магнітоопору, так і на величини магнітного поля, що відповідають максимумам магнітоопору. Широкий спектр магнітотранспортних явищ, що спостерігаються у напівметалевих композиційних матеріалах, сприяє розробці сучасних концепцій про особливості поведінки провідності біля порогу метал–ізолятор та впливу міжфазних меж метал–ізолятор на тунельну провідність.

Ключові слова: половинні метали, двоокис хрому, магнітні тунельні контакти, пресовані порошки, перколяційна провідність, анізотропія магнітоопору.